Numerical solutions of two-phase flow with applications to CO_2 sequestration and polymer flooding

Trine Solberg Mykkeltvedt

Dissertation for the degree of Philosophiae Doctor (PhD)

Department of Mathematics
University of Bergen

October 2014

Preface

This dissertation is submitted as a partial fulfillment of the requirements for the degree Doctor Philosophy (PhD) at the University of Bergen.
The advisory committee has consisted of Ivar Aavatsmark (University of Bergen, Uni research CIPR), Knut-Andreas Lie (University of Bergen, SINTEF ICT), and Helge K. Dahle (University of Bergen).

Outline

This dissertation consists of two parts. The first part provides the background theory for the papers included in the second part.

The background theory in Part I is structured as follows. First, the motivation and scope of this thesis are given in Chapter 1. Next, different properties and concepts of flow in a reservoir and the applications polymer flooding and CO_2 sequestration are introduced. The governing equations for two-phase flow and the mentioned applications are derived in Chapter 2. These equations are on the general form of hyperbolic conservation laws. General theory and background on this class of equations are given in Chapter 3. In Chapter 4 a general framework for solving hyperbolic conservation laws numerically is presented, with focus on the numerical schemes used in the included papers. Finally, in Chapter 5 the included papers found in Part II are summarized and discussed.

The four included papers in Part 2 of the thesis are:
Paper A: T.S. Mykkeltvedt, I. Aavatsmark, and S. Tveit. *Errors in the upstream mobility scheme for counter-current two-phase flow with discontinuous permeabilities.* Proceedings of ECMOR XIII, Biarritz, France, 10-13 September 2012.
Paper B: T.S. Mykkeltvedt, I. Aavatsmark, and S. Tveit. *On the performance of the upstream mobility scheme applied to counter-current two phase flow in a heterogeneous porous medium*. Paper 163581 presented at the 2013 SPE Reservoir Simulation Symposium, The Woodlands, Texas, USA, 18-20 February 2013.
Paper C: T.S. Mykkeltvedt, I. Aavatsmark, and K.-A. Lie. *Numerical aspects of polymer flood modeling.* Submitted to Computational Geosciences, and in proceedings of ECMOR XIV (2014).
Paper D: T.S. Mykkeltvedt and J.M. Nordbotten. *Estimating effective rates of convective mixing from commercial-scale injection.* Environmental Earth Sciences 2012.

Abstract

This thesis addresses challenges related to mathematical and numerical modeling of flow in porous media. To address these challenges, two applications are considered: firstly, counter-current two-phase flow in a heterogeneous porous media and secondly, polymer flooding in the context of enhanced oil recovery. Furthermore, an upscaled model for CO_2 migration is used to estimate effective rates of convective mixing from commercial-scale injection.

Numerically, the upstream mobility scheme is widely used to solve hyperbolic conservation laws. For flow in heterogeneous porous media there exists no convergence analysis for this scheme. Studies of the convergence performance of this scheme are important due to the extensive use of the upstream mobility scheme in the reservoir simulation community. We show that the upstream mobility scheme may exhibit large errors compared to the physically relevant solution when applied to a counter-current flow in a reservoir where discontinuities in the flux function are introduced through the permeability. A small perturbation of the relative permeability values can lead to a large difference in the solution produced by the upstream mobility scheme. Not only does the scheme encounter large errors compared to what is considered to be the physically relevant solution, but the solution also lacks entropy consistency.

High-resolution schemes are often used for model problems where high accuracy is required in the presence of shocks or discontinuities. Polymer flooding represents such a system and is a difficult process to model, especially since the dynamics of the flow lead to concentration fronts that are not self-sharpening. The application of modern high-resolution schemes to a system that models polymer flooding is considered and different first- and higher-order schemes are compared in terms of how the discontinuities are treated. Through numerous numerical experiments some special numerical artifacts of the polymer system are uncovered. The need of high-resolution schemes and the importance of their applicability for the polymer problem is addressed.

The process of CO_2 migration ranges over multiple scales and results in challenges when it comes to modeling and simulation of this system. This expresses the need for a upscaled model and upscaled parameters that can capture both large and small-scale spatial and temporal effects. The ongoing CO_2-injection at the Utsira formation is considered as a field-scale study for CO_2 storage. Through an upscaled model for CO_2 migration we get the first field-scale estimates of the effective upscaled convective mixing rates in this context. The findings are comparable but somewhat higher than reported in the existing literature based on fine-scale numerical simulations. Our work validates the use of numerical simulations to obtain upscaled convective mixing rates,

while at the same time validating that convective mixing is an important quantifiable storage mechanism at the Utsira formation. To account for uncertainties in the description of the storage formation, sensitivity studies are conducted relative to some of the most uncertain parameters.

Acknowledgements

I am very privileged to have a group of excellent advisors who have shared their knowledge with me. First, I would like to thank Ivar Aavatsmark for believing in me and for his constant support during my time as a PhD student. Secondly, I would like to thank my other advisor Knut-Andreas Lie for his guidance and valuable comments, and for including me in his group at SINTEF ICT, Oslo. Thirdly, I express my gratitude to Helge K. Dahle for support and encouragement during my time at the University of Bergen. Furthermore, although Jan M. Nordbotten has not officially been my advisor I am very grateful for his enthusiasm and support during my work on one of the included papers.
I would like to acknowledge my current and past colleagues in the porous media group at the University of Bergen. For both scientific and non-scientific discussions I particularly thank Eirik, Sergey, Kristian, Svenn, and Henning. I have been very lucky to share office with Elsa, thank you for everything.
Finally, I thank my family and friends for being supportive.
Especially, I thank Erik for being there all the way.

Contents

Part I

Background

Chapter 1

Introduction

Sediments and organic material were deposited in layered structures millions of years ago and formed what today are called *reservoirs* or *petroleum reservoirs*. These sediments make up the reservoir rock, whilst the deposited organic material has evolved into valuable hydrocarbons through chemical reactions. Already in the early twentieth century, crude oil was the most valuable commodity trade on world markets. Since then the technology and the petroleum industry has grown rapidly to meet the increasing global energy demand.

The process of recovering oil and gas can be divided into three stages: *primary, secondary*, and *tertiary* recovery. In the primary recovery stage the natural pressure difference between the reservoir and well is the driving force that pushes the oil to the surface. During this process the reservoir pressure decreases and only a small percentage, typically around 10% for oil reservoirs, is recovered from the rock [82]. To increase the production of oil in the secondary recovery stage, water or gas is injected to maintain the reservoir pressure and push more oil (up to 40%) out of the rock. In the tertiary recovery stage, the goal is to recover even more oil.

Enhanced oil recovery (EOR) can be achieved by injecting materials that are not naturally present in the reservoir to alter the properties of the fluids. Due to the high demand for energy and depletion of light oil, EOR techniques to recover heavy oil (crude oil with high density and high viscosity) have been investigated. Heavy oil is especially hard to recover since it has much higher viscosity than water, which will cause the water to finger through the oil and leave a large percentage of residual or non-recoverable oil behind. Chemical flooding with polymer and thermal methods such as steam flood and hot water flood are examples of common EOR techniques. Polymer flooding reduce the viscosity of injected water and is the most widely used chemical EOR technique [31].

In the early 1970s, injection of carbon dioxide (CO_2) into reservoirs started as an EOR strategy. This was a strategy to maximize profit and the injected CO_2 was taken from natural CO_2 reservoirs. More than a decade later, CO_2 injection into subsurface formations was considered for the purpose of emission avoidance. This means that CO_2 from industrial sources is captured and stored for environmental benefit, this is often referred to as CO_2 sequestration. Deep sedimentary formations are the best target for large-scale

CO_2 injections. These include depleted oil and gas reservoirs, unminable coal seams, and deep saline aquifers, see Figure 1.1. The numbers in this figure represent the following: (1) CO_2 injection in a deep saline aquifer, (2) CO_2 injection for the purpose of EOR, (3) CO_2 injection in a depleted oil reservoir, and (4) CO_2 injection in a coal seam. In 1996 the first pure CO_2 storage project started off the coast of Norway in the

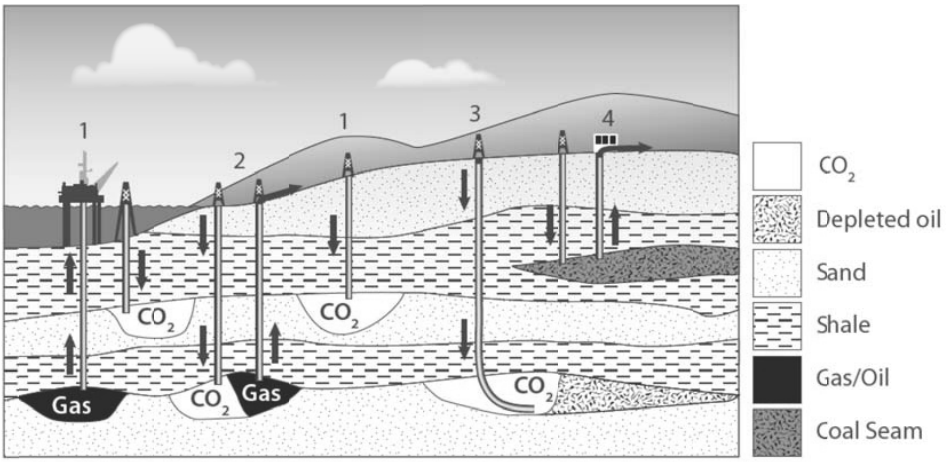

Figure 1.1: Formations suitable for geological storage of CO_2(illustration adapted from [46] and modified by [75].

Utsira formation. Over the last decade much research has been conducted on modeling approaches for this topic, [75].

Mathematical and numerical modeling of the mentioned flow systems is important to understand the dynamics of the flow. This is crucial to be able to answer practical questions and improve decision-making in real life applications. The paradox that, although the environmental consequences of oil recovery and CO_2 storage are opposite, these flow systems are modeled with the same mathematical framework and have the same modeling challenges. Mathematically, the dynamics of these operations can be modeled by a coupled system of non-linear partial differential equations. Injection of water into an oil reservoir, or injection of CO_2 into a water saturated formation, can in its simplified form be described by a system of an elliptic equation for the fluid pressure and a hyperbolic equation for the transport of the fluid phase.

To give a proper mathematical description of the flow is challenging. The modeling equations can rarely be solved analytically and one must rely on numerical approximations. The choice of mathematical description and numerical framework is thus a trade-off between accuracy, computational cost, and included complexity. Thus, the modeling of this system has several challenges. First of all, processes take place on spatial scales ranging from millimeters to several kilometers are involved. For example, the horizontal extent of the reservoirs can be several kilometers whilst the vertical extent is on the order of tens of meters. For the purpose of storing CO_2, the timescales involved range from seconds to thousands of years. Secondly, the parameters involved are highly variable and typically little or no data exists. Thirdly, the equations involved

are derived under simplifying assumptions that do not necessarily reflect the process they are modeling accurately.

Industrial and academic reservoir simulators have existed for decades, and there is still need for better numerical methods. Extended knowledge and limitations of existing methods are especially crucial to obtain.

In this contribution, mainly the hyperbolic mass-conservation equation describing the transport of the fluid phase has been studied. Note that this class of equations is also found in several other physical applications, e.g., in gas dynamics, acoustics, astrophysics, and combustion theory.

Herein, we will mainly use one-dimensional flow models to study different numerical schemes. Our results, however, will be more generally applicable since many numerical methods use one-dimensional calculations for the flux in the direction normal to the boundaries of the discretization cell. For the application of CO_2 injection, the large ratio between the horizontal and vertical extent of the aquifer has been exploited to use the study of two-dimensional flow to model the full three-dimensional system.

The main contribution of this thesis:

1. One of the classical numerical schemes (the upstream mobility scheme) used to solve hyperbolic conservation laws is shown to be erroneous and ill-conditioned for counter-current flow involving more than one rock type. This scheme is widely used and applied in most reservoir simulators. For this reason, studies of this schemes convergence performance and applicability is very important. The findings of this work show several realistic cases where this scheme can fail, and give rise to an important discussion on what the physically relevant solution of such problems is.

2. In this work, modern high-resolution schemes are applied to model polymer flooding. It is found that different initial conditions and the inclusion of adsorption and permeability reduction can change not only the solution, but also the behavior of different numerical schemes. These effects can also influence the applicability of a solver and we investigate of how suitable different numerical schemes are for different polymer flooding situations. Several numerical artifacts of this system are found, and we have quantified when these are expected to occur. Overall, the minmod slope limiter, combined with a flux approximation that exploits the solution of the Riemann problem, in the high-resolution framework is the most reliable scheme.

3. An upscaled model for CO_2 migration that includes interphase mass exchange and subsequent transport of CO_2 as a dissolved component in the aqueous phase is used to obtain the first field-scale estimates of the effective upscaled transport rate of the dissolved component (convective mixing) in the context of CO_2 storage. This work validates the use of numerical simulations to obtain upscaled convective mixing rates, while at the same time demonstrating that convective mixing is an important and quantifiable storage mechanism in the Utsira formation.

Chapter 2

Mathematical framework

This chapter consists of two main parts. Firstly, the framework and different properties of flow in a reservoir are discussed together with some applications. Secondly, the governing equations for two-phase flow and the applications used in this work are derived.

2.1 Flow in a reservoir

A reservoir is a porous geological formation that consists of solid and void space, otherwise known as a porous medium. To describe the flow in a porous medium or a reservoir we need to introduce physical properties that describe the rock, the fluid, and the interaction between rock and fluid. In many applications two or more phases are present in the pore space and for this reason theory on general *two-phase flow* is given. Extended theory and more detailed descriptions of flow in porous media are available in, e.g., [5, 13, 28].

Next, two specific applications of two-phase flow used in this work are introduced. That is, polymer flooding as an enhanced oil recovery technique and CO_2 migration in a deep saline aquifer for the purpose of storing CO_2.

2.1.1 Rock and fluid properties

The pore or void space in a porous medium consists of a three-dimensional network of channels and isolated pores where fluid can be present. We distinguish between the effective or interconnected pore space, which forms a continuous void space within the porous medium, and the isolated or non-interconnected pores. The porous structure is not visible to the naked eye and a detailed description of the void space is not available. Thus, the porous medium is treated as a continuum and we rely on macroscopic parameters to describe the flow. These parameters are defined on a small volume called a representative elementary volume (REV) [13].

The ratio of the total volume of the pores, excluding the isolated pores, and the total volume defines the effective *porosity* of the medium, from now on referred to as the porosity and denoted by ϕ.

The *absolute permeability* of the rock describes the flow conductivity of the rock and is mostly determined experimentally. The SI-unit of absolute permeability is [m^2] but a more practical unit is the *darcy* (1 darcy $\approx 9.869233 \cdot 10^{-12} m^2$) in honor of the French engineer Henry Darcy. Since the absolute permeability can vary in different directions, this is called anisotropic, it is described by a tensor $\mathbf{K}$, which according to Onsager's principle is symmetric and positive definite. In this work we have mostly considered one-dimensional or isotropic fluid flow. That is, flow with no directional preferences. Another common simplification is to consider the absolute permeability as constant (homogeneous) across the domain. However, most realistic reservoirs have a varying (heterogeneous) permeability field.

A fluid phase has a *density* ρ, which is mass of fluid per unit volume with units of [kg/m^3] in the SI system. The density of a phase can vary with, for example, temperature and pressure. Each phase has a viscosity μ which represents the internal resistance to flow. For example, usually water has a low while oil has high viscosity. The SI-unit for viscosity is [Pa s] = [kg/ms] and the viscosity can vary with pressure and molar composition, while also being highly temperature dependent.

The *compressibility* $\tilde{c}$ of a fluid or a rock is the measure of change in volumes due to change in pressure

$$\tilde{c} = \frac{1}{\rho}\frac{\partial \rho}{\partial p}.$$

The compressibility of an ideal fluid is constant. Often, we make the assumption that the fluid is incompressible, that is $\tilde{c} = 0$ and thus the density of the fluid is constant. This simplification is not physically valid, however it is very common as it simplifies analysis and implementation of the problem.

Earlier, the practical unit of Darcy was introduced for the absolute permeability. In 1856 Henry Darcy discovered an empirical relationship for water flow in porous media through experiments. This relationship establishes that the volumetric flow rate is a function of the flow area, elevation, pressure and a proportionality constant. The relationship is given in several different equivalent forms depending on the flow conditions. In this work, and for applications in reservoir engineering, the following differential form is mostly used

$$\mathbf{v} = -\frac{\mathbf{K}}{\mu}\left(\nabla p - \rho \mathbf{g}\right), \tag{2.1}$$

where $\mathbf{v}$ is the *Darcy velocity*, $\mathbf{K}$ is the absolute permeability, μ is the viscosity, p the pressure, ρ the density, and $\mathbf{g}$ a vector in the direction of gravity (i.e., downward). This relationship was later shown to be valid for any Newtonian fluid [13].

Multi-phase flow

When water or CO_2 is injected into a subsurface formation, the injected fluid initially exists as a separate fluid phase. At the pore-scale, fluid-fluid interfaces will be present that allow two phases to coexists in the pore space and the formation consists of two phases. This gives more complicated physics and chemistry of the problem, and results in a complicated mathematical description. For practical applications it is necessary to represent pore-scale processes through parameters defined on larger scales.

If the fluid in a reservoir exists in several phases there are several parameters that need to be defined. The *saturation* of a phase α, denoted by s_α, is the ratio between the volume occupied by that phase compared to the effective volume of the pores. Since the pore space must always be completely filled with fluids, we have the relation $\sum_{\forall\alpha} s_\alpha = 1$.The *residual saturation* of phase α is the minimum saturation that is attainable for that phase when displaced by another phase and is denoted by $s_{r\alpha}$.

A phase α has the pressure denoted by p_α. In general, a pressure difference exists across the interface separating two phases. The magnitude of the pressure difference depends on the curvature of this interface. One of the phases will be called the *wetting* phase, and one will be called the *non-wetting* phase. In general, the phase that has the smaller contact angle with the rock is the wetting phase and the phase with larger contact angle is the non-wetting phase. For a system with water and oil, the two phases corresponds to the wetting and the non-wetting phase, respectively.

The difference in the phase pressures between the wetting and the non-wetting phase is called the *capillary pressure*, and is denoted by P_C,

$$P_C = p_n - p_w,$$

where subscript n and w indicate the phase pressure of the non-wetting and wetting phase, respectively. The capillary pressure P_C depends on saturation and on the geometry in which the phase interface occurs, with P_C being larger in small spaces than in large spaces for a given saturation [17].

If one phase is displaced by another, we distinguish between *imbibition* and *drainage*. Imbibition is the displacement of a non-wetting by a wetting phase. Drainage is displacement of a wetting by a non-wetting phase.

If two or more phases are present and can mix with each other we say that the phases are *miscible*. On the contrary, *immiscible* phases do not mix with one another. If two phases are present, a new factor is introduced into Darcy's law (2.1), to reduce the apparent permeability. This factor, called the *relative permeability*, accounts for the reduction in apparent permeability for one phase as a result of the presence of the other phase. The relative permeability of phase α is dependent of the saturation of that phase s_α, and denoted by $k_{r\alpha}(s_\alpha)$. The Darcy velocity of phase α is

$$\mathbf{v}_\alpha = -\boldsymbol{\lambda}_\alpha \left(\nabla p_\alpha - \rho_\alpha \mathbf{g}\right), \tag{2.2}$$

where ρ_α and p_α is the density and pressure of phase α. Furthermore, $\boldsymbol{\lambda}_\alpha$ is the

mobility of phase α given by

$$\boldsymbol{\lambda}_\alpha(s_\alpha) = \mathbf{K}\frac{k_{r\alpha}(s_\alpha)}{\mu_\alpha},$$

and μ_α is the viscosity of phase α. The relationship between saturation and relative permeability is essential when modeling two-phase flow. However, to find this relation is a non-trivial task. Both the relative permeability and the previously introduced capillary pressure are caused by interface tension, and must be defined in a consistent manner. For two-phase flow there are several models partly based on data from laboratory experiments. In the included papers, mainly the Brooks-Corey and van Genuchten relative permeability functions given in [17] and [91], respectively, are used. To state these relationships, the *normalized water saturation* is introduced:

$$s_{wn} = \frac{s_w - s_{rw}}{1 - s_{rw} - s_{rn}}.$$

The Brooks-Corey relative permeabilities are given by

$$\begin{aligned} k_{rw}(s_w) &= s_{wn}^{(2+3l)/l}, \\ k_{rn}(s_w) &= (1 - s_{wn})^2(1 - s_{wn}^{(2+l)/l}), \end{aligned} \tag{2.3}$$

where l is an index representing pore-size distribution of the medium. Furthermore, the van Genucthen relative permeabilities are given by

$$\begin{aligned} k_{rw}(s_w) &= \bar{k}_1 \left[s_w^{1/2} \left(1 - \left(1 - s_w^{1/m} \right)^m \right)^2 \right], \\ k_{rn}(s_w) &= \bar{k}_2 \left[s_w^{1/2} \left(1 - (1 - s_w)^{1/m} \right)^{2m} \right]. \end{aligned} \tag{2.4}$$

where m is an empirical coefficient for the porous medium, and $\bar{k}_1$ and $\bar{k}_2$ are coefficients representing the end-points of the relative permeability curves. Relative permeability curves can also be found through interpolation on a given dataset of relative permeability values.

Sometimes we are not only interested in the overall phase, but in one or more of the *components* that make up that phase. Components migrate from one phase to another through mass transfer mechanisms. A component in a phase is denoted by superscript j and the concentration of that component is defined as the mass fraction of phase α

$$m_\alpha^j = \frac{\text{mass of the component } j \text{ in phase } \alpha}{\text{total mass in phase } \alpha}.$$

For two of the applications used in this work, one or more of the phases can consist of several components. This will be elaborated on when the applications are introduced.

2.1.2 Polymer flooding

A polymer is a water solute added to the water to increase its viscosity. This enhances the water's ability to push oil through the rock because of a more favorable mobility-ratio between the injected and displaced fluids. This results in a better sweep efficiency.

For a more detailed description of the chemistry involved in polymer flooding, see, e.g., [61].

When considering polymer flooding, there are several properties that can affect the flood. Smaller portions of the pore space will not allow polymer molecules to enter because of their size. This volume is called the *inaccessible pore volume*. Thus, a portion of the total pore space is inaccessible to the polymer and the polymer flow is accelerated. This volume depends on the molecular weight, porosity, and pore size distribution. In extreme cases, this space can be up to 30% of the total pore space.

During polymer flooding through a reservoir there is usually *adsorption* of polymer molecules onto the reservoir rock surface, this is illustrated in Figure 2.1. Adsorption decreases the polymer concentration and consequently the viscosity in the water flood. Thus, adsorption represents a net reduction in the polymer slug. The adsorption depends on many factors, such as polymer concentration, polymer type, pH, salinity, ionic strength, and reservoir heterogeneity. This and consequences of the adsorption for the polymer flooding has been studied in the literature, see, e.g., [27] and the references therein. At constant temperatures, an adsorption isotherm gives a relation between the

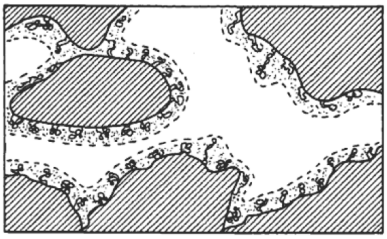

Figure 2.1: Adsorption of polymer onto the pore walls, illustration adapted from [27].

amount of adsorbed polymer and the polymer concentration c. The Langmuir isotherm theory is a favorable tool for modeling the polymer adsorption process. For a given rock, the polymer adsorption is represented by a Langmuir type isotherm

$$c_s = \frac{ac}{1+bc},$$

where c and c_s are the polymer concentration in the water and on the rock phases, respectively. The term b controls the curvature of the isotherm, and the ratio a/b denotes the plateau value for adsorption. Typical adsorption isotherms are quite steep and attain their plateau value for a very low polymer concentration c.

Adsorption onto the pore walls shrinks the pores. Thus the permeability of the rock can be reduced, and studies indicate that the relative permeability of the water is reduced as a consequence of this [77]. This reduction in water permeability can be modeled by a reduction factor $R(c)$, given by

$$R(c) = 1 + (\mathrm{RRF} - 1)\frac{a(c)}{a_{\max}}, \tag{2.5}$$

where $\mathrm{RRF} \geq 1$ is called the residual resistance factor and $a_{\max}$ is the maximum adsorption.

In Section 2.2.2 a set of equations modeling polymer flooding including adsorption and permeability reduction is derived.

2.1.3 Geological storage of CO_2

Geological storage of CO_2 is considered to be the most realistic short-term solution to reduce emissions of CO_2 to the atmosphere. A formation in the deep subsea that has advantageous conditions to inject CO_2 has temperature and pressure conditions that cause CO_2 to be compressed to a supercritical state, that is $p_n > 7.38$ MPa and $T > 31.1^{\circ}$C. Note that such a deep saline aquifer is initially saturated with *brine* (salty water).

Supercritical CO_2 is less dense than the formation brine and this leads to upward movement of CO_2 displacing brine, driven by buoyancy that produces strong gravity segregation. This is often referred to as a gravity override. As CO_2 dissolves into the brine, the resulting CO_2-saturated brine is more dense than the original brine, leading to a density-driven convection pattern. There are different mechanisms that contribute to the process of dissolution. Firstly, there is diffusion of CO_2 in the brine phase, which allows more CO_2 to dissolve in brine. Secondly, dissolution of CO_2 into brine induces an increase in the brine phase density. Though small, this density increase creates a gravitationally unstable convection of brine saturated with CO_2 above less dense brine, which can transport CO_2 downward while driving brine with low CO_2 concentration upward. This convection is called *convective mixing* and the mechanism accelerates the rate at which CO_2 is dissolved.

Primary trapping mechanisms in the context of long term storage-security are considered to be those of *structural*, *capillary*, and *solubility* trapping [12]. Structural trapping refers to low-permeable barriers in the large-scale topography, which is a prerequisite for any potential storage site. Furthermore, capillary trapping is the immobilization of CO_2 in residual state due to interfacial tension between free-phase CO_2 and brine that prevent further upward movement and thus immobilizes the CO_2. This is a local effect on the centimeter and meter spatial scales. Finally, solubility trapping is the dissolution of CO_2 into the formation brine. The convection-patterns that arise generate trapping on the scale of the thickness of the aquifer. Thus, the contribution of the different trapping mechanisms depends on several physical processes that are active on varying spatial and temporal scales and makes the problem challenging to model accurately.

2.2 Governing equations

In this section we derive the governing equations for the different applications used in this work. First, the classical mass-conservation equation for two-phase flow, which is used in papers A and B, is given. Next, an extension of this to a pair of equations modeling polymer flooding used in Paper C is given. Finally, the mathematical framework used to model CO_2 migration in a saline aquifer used in Paper D is given.

2.2.1 Two-phase flow

The mass-conservation equations for two-phase immiscible flow are given by

$$(\phi \rho_\alpha s_\alpha)_t + \nabla \cdot (\rho_\alpha \mathbf{v}_\alpha) = 0, \qquad \text{and} \qquad \alpha = w, n \tag{2.6}$$

where subscripts $\alpha = w$ and $\alpha = n$ represent the wetting and non-wetting phase, respectively, ϕ denotes the porosity, and ρ_α denotes the density of phase α. Furthermore, s_α and $\mathbf{v}_\alpha$ represent the saturation and the velocity of phase α. Now, assume that the flow is incompressible. Thus, (2.6) reduces to

$$\phi \, (s_\alpha)_t + \nabla \cdot \mathbf{v}_\alpha = 0. \tag{2.7}$$

The velocity of phase α is given by Darcy's law (2.2), and the sum of the phase saturations has the relation

$$s_w + s_n = 1. \tag{2.8}$$

Thus, adding the mass-conservation equations (2.7) for both phases, using (2.8), and let $\mathbf{v}(t) = \mathbf{v}_w + \mathbf{v}_n$ be the total velocity, we obtain

$$\begin{aligned} \nabla \cdot \mathbf{v} &= 0, \\ \nabla \cdot (\mathbf{v}_w + \mathbf{v}_n) &= 0. \end{aligned} \tag{2.9}$$

Next, use Darcy's law (2.2) and consider $(\boldsymbol{\lambda}_n \mathbf{v}_w - \boldsymbol{\lambda}_w \mathbf{v}_n)$ to obtain an isolated expression for $\mathbf{v}_w$ using (2.9),

$$\mathbf{v}_w = \frac{\boldsymbol{\lambda}_w}{\boldsymbol{\lambda}_w + \boldsymbol{\lambda}_n} \left(\mathbf{v} + \boldsymbol{\lambda}_n \left(\nabla P_C + (\rho_w - \rho_n) \, \mathbf{g} \right) \right), \tag{2.10}$$

where $P_C = p_n - p_w$ is the capillary pressure. Similarly, consider $(\boldsymbol{\lambda}_w \mathbf{v}_n - \boldsymbol{\lambda}_n \mathbf{v}_w)$ and obtain an isolated expression for $\mathbf{v}_n$

$$\mathbf{v}_n = \frac{\boldsymbol{\lambda}_n}{\boldsymbol{\lambda}_n + \boldsymbol{\lambda}_w} \left(\mathbf{v} + \boldsymbol{\lambda}_w \left(-\nabla P_C + (\rho_n - \rho_w) \, \mathbf{g} \right) \right). \tag{2.11}$$

In many reservoir problems the capillary pressure gradient is small compared to the fluid pressure gradient, and is is common to neglect P_C. We neglect the capillary pressure P_C, consider (2.7) for the wetting phase, and let the relative permeabilities $k_{r\alpha} = k_{r\alpha}(s_w)$ and, consequently, the mobilities $\boldsymbol{\lambda}_\alpha = \boldsymbol{\lambda}_\alpha(s_w)$. Then, combining (2.7) and (2.10), a mass-conservation equation for the wetting phase is obtained

$$\begin{aligned} \phi \, (s_w)_t + \nabla \cdot \mathbf{f}(s_w) &= 0, \\ \mathbf{f}(s_w) = \frac{\boldsymbol{\lambda}_w}{\boldsymbol{\lambda}_w + \boldsymbol{\lambda}_n} &\left(\mathbf{v} + \boldsymbol{\lambda}_n \left(\rho_w - \rho_n \right) \mathbf{g} \right), \end{aligned} \tag{2.12}$$

where $\mathbf{f}$ is called the flux function. This equation is also called the *saturation equation* or *factional flow formulation*.

Similarly, let the relative permeabilities $k_{r\alpha} = k_{r\alpha}(s_n)$ and, consequently, the mobilities $\boldsymbol{\lambda}_\alpha = \boldsymbol{\lambda}_\alpha(s_n)$. Then, combine (2.7) and (2.11) to obtain the mass-conservation equation for the non-wetting phase

$$\begin{aligned} \phi\,(s_n)_t + \nabla\cdot\mathbf{f}(s_n) &= 0, \\ \mathbf{f}(s_n) &= \frac{\boldsymbol{\lambda}_n}{\boldsymbol{\lambda}_n+\boldsymbol{\lambda}_w}\left(\mathbf{v}+\boldsymbol{\lambda}_w(\rho_n-\rho_w)\mathbf{g}\right). \end{aligned} \tag{2.13}$$

The one-dimensional version of the mass-conservation equation for the wetting phase (2.12) was studied by Buckley and Leverett in 1942 [18] for this simplified two-phase flow problem, and has since been devoted remarkably much attention. This formulation is often referred to as the Buckley-Leverett equation. The one-dimensional version of the mass-conservation equation for the wetting (2.12) that models two-phase flow, is given by

$$\begin{aligned} \phi(s_w)_t + f(s_w)_x &= 0, \\ \text{with} \qquad f(s_w) &= \frac{\lambda_w}{\lambda_w+\lambda_n}\left(v \pm \lambda_n(g_w-g_n)\right), \end{aligned} \tag{2.14}$$

where $g_\alpha = \rho_\alpha g\cos(\theta)$ with $\alpha = w,n$ denoting the influence of gravity at the angle θ from the vertical axis. Note that the sign in front of the gravity term, $\lambda_n(g_w-g_n)$, depends on the type of flow we are considering, see Figure 2.2. Particularly, let $\mathbf{e}_1$ be aligned with the x-direction of the flow, thus the gravity vector $\mathbf{g}$ has the component $-g\cos(\theta)$ and $g\cos(\theta)$ in the $\mathbf{e}_1$ direction for up-dip and down-dip flow, respectively, see Figure 2.2. This means that the sign is positive for down-dip flow and negative for up-dip flow.

(a) Horizontal flow. (b) Up-dip flow flow. (c) Down-dip flow.

Figure 2.2: Directions of the one-dimensional flow.

2.2.2 Polymer flooding

When a polymer is added to water it is assumed that the water and polymer coexist in the aqueous phase while the oil forms its own liquid phase. Thus, the polymer flooding consists of two phases and three components. The mass-conservation equations for the three components oil, water, and polymer, read

$$(\phi\rho_n s_n)_t + \nabla\cdot(\rho_n\mathbf{v}_n) = 0, \tag{2.15a}$$
$$(\phi\rho_w s_w)_t + \nabla\cdot(\rho_w\mathbf{v}_w) = 0, \tag{2.15b}$$
$$(\phi\rho_w s_w c + (1-\phi_r)\rho_r\bar{a}(c))_t + \nabla\cdot(\rho_w c\mathbf{v}_{wp}) = 0, \tag{2.15c}$$

where c is the polymer concentration. In (2.15c), ρ_r is the reference rock density, ϕ_r the reference porosity, and $\bar{a}(c)$ represents the amount of polymer adsorbed by the rock, only dependent on the polymer concentration c. Here, $\mathbf{v}_{wp}$ is the velocity of water containing polymer. The reservoir rock is now assumed to be homogeneous, thus the porosity and the total permeability of the rock are constant. The phases are assumed to be incompressible such that ρ_α is constant. Thus, Equations (2.15a-2.15c) reduce to

$$(s_n)_t + \nabla \cdot \mathbf{v}_n = 0, \tag{2.16a}$$

$$(s_w)_t + \nabla \cdot \mathbf{v}_w = 0, \tag{2.16b}$$

$$\left(s_w c + \frac{1-\phi_r}{\phi} \frac{\rho_r}{\rho_w} \bar{a}(c) \right)_t + \nabla \cdot (c \mathbf{v}_{wp}) = 0. \tag{2.16c}$$

The phase velocities $\mathbf{v}_\alpha$ are given by Darcy's law (2.2), the relative permeabilities are $k_{r\alpha} = k_{r\alpha}(s_w)$, and the mobilities $\boldsymbol{\lambda}_\alpha$ for the polymer system are

$$\boldsymbol{\lambda}_w = \mathbf{K} \frac{k_{rw}(s_w)}{\mu_w(c)} \frac{1}{R(c)}, \qquad \text{and} \qquad \boldsymbol{\lambda}_n = \mathbf{K} \frac{k_{rn}(s_w)}{\mu_n}. \tag{2.17}$$

In (2.17) $R(c)$ models the reduction in permeability of the rock to the water phase due to adsorption. This can be modeled by (2.5). Here, it is assumed that the viscosity of oil is constant, and that the viscosity of the water phase increases as the concentration of the polymer increases. It is assumed that the polymer does not affect the pressure and density, and that the relative permeability does not depend on mixing. Thus, the velocity $\mathbf{v}_{wp}$ is given by

$$\begin{aligned} \mathbf{v}_{wp} &= -\boldsymbol{\lambda}_{wp} (p_w - \rho_w \mathbf{g}), \\ \text{where} \qquad \boldsymbol{\lambda}_{wp} &= \mathbf{K} \frac{k_{rw}(s_w)}{\mu_p(c) R(c)}. \end{aligned}$$

Hence,

$$\mathbf{v}_{wp} = m(c) \mathbf{v}_w, \qquad \text{where} \qquad m(c) = \frac{\mu_w(c)}{\mu_p(c)},$$

and $m(c)$ is called the polymer mobility factor. This factor equals 1 if the polymer is fully mixed in water. A representation that includes the degree of mixing can be found in, e.g., [86].

Now, let the total velocity be given by $\mathbf{v} = \mathbf{v}_w + \mathbf{v}_n$ and obtain an isolated expression for $\mathbf{v}_w$ similar to (2.10). For simplicity we neglect the capillary pressure P_C, set the porosity $\phi = 1$, and let $a(c) = \frac{\rho_r}{\rho_w \bar{a}(c)}$. Then, the mass-conservation equation for the aqueous phase (2.16b) can be written as

$$(s_w)_t + \nabla \cdot \mathbf{f}(s_w, c) = 0, \tag{2.18a}$$

and similarly the mass-conservation equation for the polymer component (2.16c) can be written as

$$(s_w c + a(c))_t + \nabla \cdot (c \mathbf{f}(s_w, c)) = 0. \tag{2.18b}$$

In (2.18a) and (2.18b) the flux function $\mathbf{f}(s_w, c)$ of the system is given by

$$\mathbf{f}(s_w, c) = \frac{\boldsymbol{\lambda}_w}{\boldsymbol{\lambda}_w + \boldsymbol{\lambda}_n} \left(\mathbf{v} + \boldsymbol{\lambda}_n(\rho_w + \rho_n)\mathbf{g}\right).$$

In one dimension the mass-conservation equations (2.18a) and (2.18b) make up the system

$$\begin{aligned} (s_w)_t + f(s_w, c)_x &= 0, \\ (s_w c + a(c))_t + c f(s, c)_x &= 0, \end{aligned} \tag{2.19}$$

where the one-dimensional flux function is given by

$$f(s_w, c) = \frac{\lambda_w}{\lambda_w + \lambda_n} \left(v \pm \lambda_n(g_w - g_n)\right). \tag{2.20}$$

Note that the sign in front of the gravity term, $\lambda_n(g_w - g_n)$, depends on the type of flow we are considering, see Figure 2.2.

To emphasize the influence the polymer concentration c and the permeability reduction $R(c)$ have on the flux function $f(s, c)$ a simple example is considered. Assume down-dip flow and let $g_w = 2$, $g_n = 1$, $v = 0.2$, $\lambda_w = s^2/(0.5 + c)$, and $\lambda_n = (1 - s)^2$. The corresponding flux functions for different values of c are shown in Figure 2.3. Similarly, for polymer concentration $c = 1$, the flux functions for different permeability reduction functions $R(c)$ are shown in Figure 2.4.

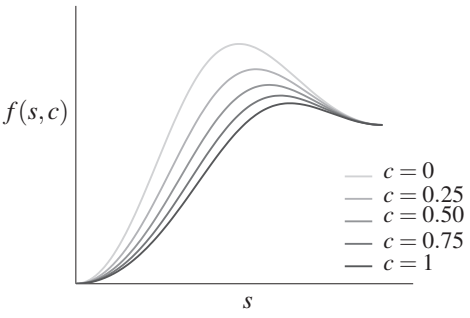

Figure 2.3: Flux function $f(s, c)$ for different values of the polymer concentration c for saturation values $s \in [0, 1]$. Increasing polymer concentration for darker grey.

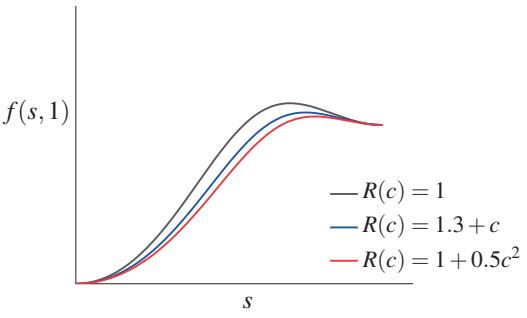

Figure 2.4: Flux function $f(1, s)$ for polymer concentration $c = 1$ and different permeability reduction functions $R(c)$.

2.2.3 CO_2 migration

In Section 2.1.3 the different trapping mechanisms for CO_2 migration were described. The flow consists of two fluid phases and the following model was first presented and discussed in detail in [32, 33, 75].

Permeable subsurface formations often have a horizontal extent on the order of tens to hundreds of kilometers, whilst the vertical extent is on the order of tens to hundreds of meters. In many applications, this disparity in length scales can be taken advantage of. Within such formations the vertical flows are considered to be small compared to the horizontal flows, and can thus be neglected. This assumption is strengthened by the *tangent law of flow* which says that along the boundary separating a high-permeable and a low permeable formation, the flow of the high-permeable formation is parallel to the boundary, and the flow of the low-permeable formation is normal to the relative interface. This motivates the approach of simplifying the governing equations of the flow to only focus on horizontal flow. Models based on this approach are called *vertically integrated models* and are derived by integrating the governing equations over the vertical dimension, thus eliminating the vertical coordinate and subsequently transforming the relevant variables into integrated quantities independent of the vertical coordinate. These models have historically been considered in the context of oil recovery [23, 71]. However, over the last decade, these models have received renewed attention in the context of geological storage of CO_2 [21, 33, 42, 54, 74, 76].

Now, we mention some of the simplifications that can make the CO_2 migration a more tractable problem to model. This involves capturing both large and small-scale spatial and temporal effects. Firstly, the density difference between the CO_2 and brine leads to a strong macroscopic tendency to be separated by gravity. Thus, it is assumed that these regions are separated by a macroscopic sharp interface. One approach where the consequences of this assumption is investigated, can be found in [76]. Secondly, a saline aquifer suitable for injection of CO_2 is a typical application where the horizontal extent is much larger than the vertical extent and a vertically integrated approach can be applied. This is a valid assumption since the timescale of gravity segregation is fast compared to the typical timescale of the overall horizontal flow of a CO_2-brine system. Extended theory on the subject of gravity-segregated flow both with and without the sharp interface assumption can be found in, e.g., [23, 32, 45, 61, 96]. Finally, changes in density and viscosity as a function of changing pressure and thermal effects can be ignored, therefore no energy balance equation needs to be written.

The vertical equilibrium assumption essentially says that the flow in the vertical direction is negligible. That is, the flow perpendicular to the formation is negligible

$$\mathbf{v}_\alpha \cdot \mathbf{e}_3 = -\lambda_{\alpha,3}(s_\alpha)\left(\frac{\partial p_\alpha}{\partial x_3} - \rho_\alpha \mathbf{g}\cdot\mathbf{e}_3\right). \tag{2.21}$$

It is assumed that x_3 is aligned with the direction of one of the principle components of mobility

$$\boldsymbol{\lambda}_\alpha = \begin{bmatrix} \boldsymbol{\lambda}_{\alpha,||} & \mathbf{0} \\ \boldsymbol{\lambda}_{\alpha,||} & \lambda_{\alpha,3} \end{bmatrix}$$

If the dependence of pressure on x_3 is defined by the expression in the parenthesis in (2.21), we assume that (2.21) is equal to zero, and we integrate from the pressure datum

surface ζ_p. The appropriate expression is then given by

$$\begin{aligned} 0 &= \int_{\zeta_p}^{x_3} \left(\frac{\partial p_\alpha}{\partial x_3'} - \rho_\alpha \mathbf{g} \cdot \mathbf{e}_3 \right) \, \mathrm{d}x_3', \\ p_\alpha(x_3) - p_\alpha(\zeta_p) &= (\mathbf{g} \cdot \mathbf{e}_3) \int_{\zeta_p}^{x_3} \rho_\alpha \, \mathrm{d}x_3', \end{aligned} \tag{2.22}$$

which from now on is referred to as the Dupuit reconstruction of the pressure. Note that when the density is constant in the vertical direction, the pressure becomes a linear function of x_3.

Now, some notation on the macroscopic regions in the system of CO_2 and brine are given. Let the topography of the impermeable cap rock be described by the interface $x_3 = \zeta_T(\mathbf{x})$, where $\mathbf{x}$ is the horizontal location. The bottom of the aquifer is described by the interface $x_3 = \zeta_B(\mathbf{x})$. As the plume migrates brine will displace the CO_2 in the back end of the plume and a region with residually or capillary trapped CO_2 will be created. The interface between the mobile CO_2 and the residually trapped CO_2 is in this model considered to be sharp and is denoted by $x_3 = \zeta_M(\mathbf{x})$. From these macroscopic regions we allow CO_2 to dissolve in the underlying brine and form a diffusive boundary layer that grows with time. While on the fine scale this layer is unstable, we model at the macroscopic interface, which can be conceptualized as a characteristic depth of the density-driven fingers, denoted by $x_3 = \zeta_D((x))$. The described macroscopic interfaces obey the ordering $\zeta_B \leq \zeta_D \leq \zeta_R \leq \zeta_M \leq \zeta_T$, see Figure 2.5.

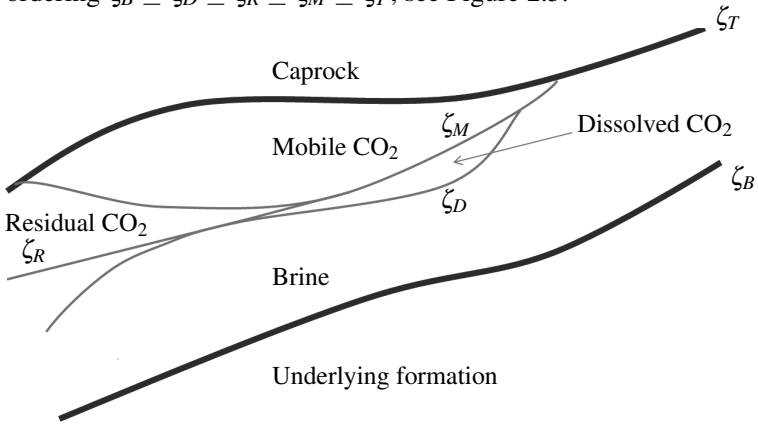

Figure 2.5: A schematic of a two-dimensional cross-section of the sharp interface model that includes solubility trapping, where the macroscopic regions are separated by the interfaces ζ_B, ζ_D, ζ_R, ζ_M, and ζ_B. The schematic is reproduced from [75].

As before, we indicate the wetting (brine) and the non-wetting (CO_2) phase with subscript w and n, respectively. In addition, to separate the two components, the superscripts w and n for the brine and CO_2 components are introduced, respectively. The density of the free phase α is denoted ρ_α^{pure}, where $\alpha = n, w$ for CO_2 and brine, respectively. The density of brine saturated with CO_2 is denoted by ρ_w^{mix}, and similarly, the

density of CO_2 saturated with brine is denoted by ρ_n^{mix}. The mass fraction of component j in phase α is denoted by m_α^j. Thus, the mass fraction of the CO_2 component in the brine phase is denoted by m_w^n, and similarly, the mass fraction of the brine component in the CO_2 phase is denoted by m_n^w.

The vertically integrated mass per unit area M^j of component j is the sum of the contribution from the free and dissolved phases. In Table 2.1 we have summarized the saturations s_α and the density of the pure and dissolved component for each phase in each of the four regions in the sharp interface model. Note that the CO_2 phase only has a contribution in the two topmost regions.

Table 2.1: Schematic of saturation and distribution of pure and dissolved components, both in the non-wetting CO_2 and the wetting brine phase, in all four regions.

	CO_2-phase			Brine-phase		
x_3	s_n	pure	dissolved	s_w	pure	dissolved
$\in (\zeta_M, \zeta_T]$	$(1-s_{rw})$	$\rho_n^{mix} m_n^n$	$\rho_n^{mix} m_n^w$	s_{rw}	$\rho_w^{mix} m_w^w$	$\rho_w^{mix} m_w^n$
$\in (\zeta_R, \zeta_M]$	s_{rn}	$\rho_n^{mix} m_n^n$	$\rho_n^{mix} m_n^w$	$(1-s_{rn})$	$\rho_w^{mix} m_w^w$	$\rho_w^{mix} m_w^n$
$\in (\zeta_D, \zeta_R]$	0			1	$\rho_w^{mix} m_w^w$	$\rho_w^{mix} m_w^n$
$\in [\zeta_B, \zeta_D]$	0			1	ρ_w^{pure}	

Thus, we can sum the contribution to each component and get the vertically integrated mass per unit area of each component

$$
\begin{aligned}
M^w &= \phi \Big(\left(\rho_w^{mix} m_w^w s_{rw} + \rho_n^{mix} m_n^w (1-s_{rw})\right)(\zeta_T - \zeta_M) + \\
&\qquad \left(\rho_w^{mix} m_w^w (1-s_{rn}) + \rho_n^{mix} m_n^w s_{rn}\right)(\zeta_M - \zeta_R) + \rho_w^{mix} m_w^w (\zeta_R - \zeta_D) + \rho_w (\zeta_D - \zeta_B) \Big), \\
M_w^n &= \phi \rho_w^{mix} m_w^n \Big(s_{rw}(\zeta_T - \zeta_M) + (1-s_{rn})(\zeta_M - \zeta_R) + (\zeta_R - \zeta_D) \Big), \\
M^n &= M_w^n + \phi \rho_n^{mix} m_n^n \left((1-s_{rw})(\zeta_T - \zeta_M) + s_{rn}(\zeta_M - \zeta_R) \right).
\end{aligned}
$$

The total mass per area of the two components j is conserved,

$$
\left(M^j\right)_t + \nabla \cdot \mathbf{F}^j = Q^j, \tag{2.23}
$$

where Q^j represents source or sink terms, and $\mathbf{F}^j$ is the vertically integrated mass flux of component j. The total mass flux of component j is the sum of the vertically integrated phase fluxes $\mathbf{v}_\alpha$,

$$
\mathbf{F}^j = \sum_\alpha \int_{\zeta_B}^{\zeta_T} \rho_\alpha m_\alpha^j \mathbf{v}_\alpha \, \mathrm{d}z.
$$

The phase fluxes $\mathbf{v}_\alpha$ are again given by Darcy's law (2.2). However, due to pressure and density differences, $\mathbf{v}_\alpha$ are different in each of the regions in the sharp interface model. To obtain an expression for $\mathbf{v}_\alpha$ in each of the regions, we use the Dupuit pressure reconstruction (2.22)

$$p_w(z) = \begin{cases} p_w(\zeta_D) + (\mathbf{g}\cdot\mathbf{e}_3)\rho_w^{mix}(z-\zeta_D), & z > \zeta_D, \\ p_w(\zeta_p) + (\mathbf{g}\cdot\mathbf{e}_3)\rho_w^{pure}(z-\zeta_p), & z \le \zeta_D, \end{cases}$$

$$p_n(z) = p_w(\zeta_M) + (\mathbf{g}\cdot\mathbf{e}_3)\rho_n^{mix}(z-\zeta_p), \qquad z \ge \zeta_M,$$

where the pressure datum interface $\zeta_p \le \zeta_D$. In the region of mobile CO_2, the free brine phase is only present in a residual state and thus $\mathbf{v}_w = 0$ in this region. Similarly, the CO_2 is only mobile when $x_3 \in (\zeta_M, \zeta_T]$ and $\mathbf{v}_n = 0$ elsewhere. For the remaining regions we have

$$\mathbf{v}_w = \begin{cases} -\boldsymbol{\lambda}_w(1)\Big(\nabla P - (\mathbf{g}\cdot\mathbf{e}_3)\rho_w^{pure}\nabla\zeta_p - \rho_w^{pure}\mathbf{g}\Big), & x_3 \in [\zeta_B, \zeta_D], \\ -\boldsymbol{\lambda}_w(1)\Big(\nabla P + (\mathbf{g}\cdot\mathbf{e}_3)\Big[\rho_w^{pure}\nabla(\zeta_D-\zeta_p) - \\ \qquad\qquad \rho_w^{mix}\nabla\zeta_D\Big] - \rho_w^{pure}\mathbf{g}\Big), & x_3 \in (\zeta_D, \zeta_R], \\ -\boldsymbol{\lambda}_w(1-s_{rn})\Big(\nabla P + (\mathbf{g}\cdot\mathbf{e}_3)\Big[\rho_w^{pure}\nabla(\zeta_D-\zeta_p) - \\ \qquad\qquad \rho_w^{mix}\nabla\zeta_D\Big] - \rho_w^{pure}\mathbf{g}\Big), & x_3 \in (\zeta_R, \zeta_M], \end{cases}$$

$$\mathbf{v}_n = -\boldsymbol{\lambda}_n(1-s_{rw})\Big(\nabla P + (\mathbf{g}\cdot\mathbf{e}_3)\Big[\rho_w^{mix}\nabla(\zeta_M-\zeta_D) - \rho_w^{pure}\nabla\zeta_p - \rho_{nw}^{mix}\nabla\zeta_p\Big] - \rho_n^{mix}\mathbf{g}\Big), \qquad x_3 \in (\zeta_M, \zeta_T].$$

In addition to the equations (2.23), we need two more equations to complete the model. The vertically integrated mass, M_w^n, of the dissolved CO_2 is modeled by the transport equation

$$(M_w^n)_t + \nabla\cdot F_w^n = C_R, \tag{2.26}$$

whenever a region of dissolved CO_2 is created, i.e., $\zeta_D < \zeta_R$. In (2.26) C_R is the effective upscaled dissolution rate representing convective mixing, and the total mass flux of dissolved CO_2 , F_w^n, is given by

$$F_w^n = \rho_w^{mix} m_w^n \int_{\zeta_D}^{\zeta_R} \mathbf{v}_w \, \mathrm{d}x_3.$$

To obtain the last equation to make up this model, we consider hysteresis. It is assumed that whenever a region of residually trapped CO_2 is created, all the CO_2 dissolving into the brine originates from this region. This means that we consider the mobile CO_2 as conserved when the interfaces are separated ($\zeta_R < \zeta_M$):

$$-\phi(1-s_{rn}-s_{rw})(\zeta_M)_t + \nabla\cdot\frac{1}{\rho_n^{mix} m_n^n} F_n^n = Q^n, \tag{2.27}$$

where F_n^n is the vertically integrated mass flux for the mobile CO_2 and Q^n represents sources/sinks.

The two equations (2.23), in addition to the equations (2.26) and (2.27) complete the model for the system with the three unknown interface locations ζ_M, ζ_R and ζ_D, and the unknown datum pressure P.

Chapter 3

Hyperbolic conservation laws

The applications presented in the previous chapter are all modeled using *hyperbolic conservation laws*. In this chapter, the general theory on this class of partial differential equations (PDEs) is presented. First, a general hyperbolic conservation law is introduced, followed by a discussion on the solution of a scalar one-dimensional conservation law. Next, a spatial discontinuity in the flux function is introduced, followed by a presentation of the solution of the pair of non-linear hyperbolic conservation laws that models polymer flooding.

3.1 Introduction

In general, a conservation law states that the rate of change of a quantity U within a given domain Ω equals the flow over the boundaries $\partial\Omega$ together with the amount generated by sources or removed by sinks inside Ω. Many practical problems in science and engineering involve conserved quantities and lead to equations of this class. In gas dynamics, the non-linear *Euler equations*, which describe the dynamics of a compressible and inviscid fluid, have been studied extensively and are often used as an example when general theory on conservation laws are presented, see, e.g., [43, 67, 87].

The general system of conservation laws in integral form for n conserved quantities $U = [u_1,\ u_2,\ ..\ ,\ u_j\ ,\ ..\ ,u_n]^T$ is given by

$$\int_{\Omega} \frac{dU}{dt}\,\mathrm{d}V + \int_{\partial\Omega} H\cdot\mathbf{n}\,\mathrm{d}S = \int_{\Omega} Q\,\mathrm{d}V, \tag{3.1}$$

where $H = [h_1,\ h_2,\ ..\ ,\ h_j\ ,\ ..\ ,h_n]^T$ is the corresponding flux function of each quantity through Ω, $\mathbf{n}$ is the outward normal vector of $\partial\Omega$, and $Q = [q_1,\ q_2,\ ..\ ,\ q_j\ ,\ ..\ ,q_n]^T$ corresponds to sources or sinks of each of the n conserved quantities. By applying the divergence theorem to (3.1) we obtain

$$\int_{\Omega} \left(\frac{dU}{dt} + \nabla\cdot H - Q\right)\,\mathrm{d}V = 0.$$

This must hold for any system of quantities U, and by requiring the integrand to be equal to zero, the system of conservation laws (3.1) in differential form reads

$$U_t + \nabla \cdot H(U) = Q. \tag{3.2}$$

If the $n \times n$ Jacobian matrix $H'(U)$ of the system (3.2) is diagonalizable with real eigenvalues λ^i for each physical relevant value of U, the system is *hyperbolic*. Furthermore, if the eigenvalues λ^i are all distinct, the system is said to be *strictly hyperbolic*.

Throughout this chapter, the homogeneous one-dimensional version of (3.2) is considered. Let $(x,t) \in \mathbb{R} \times \mathbb{R}_+$ and set source/sink terms Q to zero. Thus, the general one-dimensional system of hyperbolic conservation laws,

$$U_t + H(U)_x = 0, \tag{3.3}$$

is obtained.

The one-dimensional mass-conservation equation (2.14) that models two-phase flow, is an example of a *scalar* one-dimensional hyperbolic conservation law. Scalar equations have one conserved quantity ($n = 1$). Furthermore, the two mass conservation equations in the system (2.19) presented in Section 2.2.2, model polymer flooding and represent a system of hyperbolic conservation laws. To write these equations in the general form (3.3), let

$$U = \begin{bmatrix} s \\ sc + a(c) \end{bmatrix} \qquad \text{and} \qquad H(U) = \begin{bmatrix} f(s,c) \\ cf(s,c) \end{bmatrix},$$

where s in the rest of this thesis denotes the saturation of the wetting phase $s = s_w$.

To understand more about the applications used in this work, the general theory on equations of the form (3.3) is presented. From the application of CO_2 injection in a deep saline aquifer, the modeling equations (2.23), (2.26) and (2.27) have the shape of a conservation law (3.2). However, this application is not specifically mentioned in this chapter.

3.2 Scalar conservation laws

To simplify the exposition of scalar conservation laws, let capital letters represent a system of equations, whilst lowercase letters represent a scalar equation. Thus, a general, one-dimensional and scalar hyperbolic conservation law is given by

$$u_t + h(u)_x = 0, \tag{3.4a}$$

where $(x,t) \in \mathbb{R} \times \mathbb{R}_+$. Together with the initial condition

$$u(x,0) = u_0(x), \tag{3.4b}$$

(3.4a-3.4b) is called a *Cauchy* Initial Value Problem (IVP). The *method of characteristics* can be used to find an explicit solution of this problem. Rewriting (3.4a) in

quasilinear form (a form in which the highest derivative occurs linearly), the following equation is obtained

$$u_t + h'(u)u_x = 0,$$

where $h'(u)$ is called the *characteristic speed*, and the *characteristics* are given by $x = \xi + h'(u)t$. The *classical* solution of the conservation law (3.4a) is given by

$$u(x,t) = u_0(\xi) = u_0(x - h'(u)t).$$

A classical solution is continuously differentiable. However, regardless of how smooth the initial function $u_0(x)$ is, one cannot expect to be able to define classical solutions of such non-linear conservation laws for all times t [43]. This means that discontinuities, called *shocks* or *contact discontinuities*, can occur in the solution. To allow for these solutions, *weak solutions* are introduced.

Definition 1 ***Weak solution***
A bounded and measurable function $u(x,t)$ is a weak solution of the IVP (3.4a)-(3.4b) if

$$\iint_{\mathbb{R}\times\mathbb{R}_+} [u\gamma_t + h(u)\gamma_x]\,\mathrm{d}x\mathrm{d}t + \int_{\mathbb{R}} u_0(x)\gamma(x,0)\mathrm{d}x = 0, \tag{3.5}$$

for all test functions $\gamma \in C_0^\infty(\overline{\mathbb{R}\times\mathbb{R}_+})$

With this definition, the derivatives have been moved to the test function γ. Observe that a smooth solution is also a weak solution.

3.2.1 Discontinous solutions

Now, the question is which kind of discontinuities are compatible with (3.14). To determine this, two conditions are imposed. First, to ensure that u is conserved through a shock, the *Rankine-Hugoniot* condition is defined.

Definition 2 ***Rankine-Hugoniot condition***
Let u^L and u^R denote the values of $u(x,t)$ to the left and right of the shock, respectively. Let σ denote the shock speed. Then, a weak solution of (3.4a) is only valid if

$$\sigma(u^L - u^R) = h(u^R) - h(u^L). \tag{3.6}$$

Furthermore, a weak solution is not in general unique and thus, an additional constraint is needed to chose the physically meaningful solution. This constraint is called an *admissibility criterion* or an *entropy condition* and a variety of conditions have been developed that can be applied to weak solutions of scalar hyperbolic conservation laws [67]. This name originates from gas dynamics, where the second law of thermodynamics demands that the entropy of a system must be nondecreasing. The *Lax entropy condition* is based on the second law of thermodynamics: the discontinuity can destroy, but not generate, information. Thus, characteristics can never go out of the shock, but only go into or run parallel to it.

Definition 3 ***Lax entropy condition***
For convex, scalar conservation laws, a discontinuity propagating with speed σ given by (3.6) satisfies the Lax entropy condition if

$$h'(u^L) \geq \sigma \geq h'(u^R), \tag{3.7}$$

where u^L and u^R are values of $u(x,t)$ to the left and to the right of the discontinuity, respectively.

A more general version of (3.7), that also includes non-convex scalar flux functions, is called *Oleinik's entropy condition* and is due to [78].

Definition 4 ***Oleinik's entropy condition***
A weak solution, $u(x,t)$, is an entropy solution if the shock satisfies the additional entropy condition

$$\frac{h(u)-h(u^L)}{u-u^L} \geq \sigma \geq \frac{h(u)-h(u^R)}{u-u^R}, \tag{3.8}$$

where u is between u^L and u^R, and σ again is the shock speed given by Rankine-Hugoniot (3.6).

The Oleinik entropy condition has a simple geometrical interpretation. For a shock with left value u^L and right value u^R, the shock speed σ is the slope of the line between $(u^L, h(u^L))$ and $(u^R, h(u^R))$. The slope of the line between $(u^R, h(u^R))$ and $(u, h(u))$ for any u between u^L and u^R must be less than the shock speed σ. Observe that the weaker Lax entropy condition is also obtained by letting $u \to u^L$ and $u \to u^R$ in the left and right inequalities of (3.8), respectively.

From a viscous regularization of the conservation law, the *Kružkov entropy condition* is derived in [58]. From this condition, a general weak entropy solution is defined.

Definition 5 ***Kružkov-type entropy inequality***
A weak solution $u(x,t)$ is an entropy solution if, for any test function $\gamma \in C_0^\infty(\overline{\mathbb{R}\times\mathbb{R}_+})$,

$$\iint\limits_{\mathbb{R}\times\mathbb{R}_+} [|u-c|\gamma_t + sign(u-c)(h(u)-h(c))\gamma_x]\,\mathrm{d}x\mathrm{d}t \geq 0, \tag{3.9}$$

where c is an arbitrary constant in $\mathbb{R}$.

Note that from the condition in (3.9), the Oleinik entropy condition can be derived.

3.2.2 Riemann problem

A special IVP problem called the *Riemann problem* is given by

$$\begin{aligned} u_t + h(u)_x &= 0, \\ u(x,0) &= \begin{cases} u^L, & \text{if} \quad x < 0, \\ u^R, & \text{if} \quad x > 0, \end{cases} \end{aligned} \tag{3.10}$$

where u^L (left) and u^R (right) are two constant values. Observe that the initial data has a discontinuity at $x = 0$. The solution of this problem gives valuable information on the properties of the conservation law. Knowledge of this problem is important when solving a general Cauchy problem and this problem is discussed extensively in the literature, see, e.g., [67, 87].

The solution of the Riemann problem is characterized by waves propagating from the origin with speed x/t and is found by introducing a similarity solution, i.e., a function of $\xi = x/t$ only. Let $u(x,t) = u(x/t) = u(\xi)$ in (3.10). An ordinary differential equation (ODE)

$$\begin{aligned} (h'(u) - \xi)u_\xi &= 0, \\ u(-\infty) = u^L, \qquad &\text{and} \qquad u(\infty) = u^R. \end{aligned} \tag{3.11}$$

is obtained. In (3.11), either $(h'(u) - \xi)$ or u_ξ is equal to zero. In addition to discontinuities, this gives a solution with different types of waves. The solution of the Riemann problem consists of the following waves:

a) *Constant state*. The factor $u_\xi = 0$, that is $u(\xi) = constant$.

b) *Rarefaction waves*. This is the continuous part of the solution, where $h'(u) = \xi$ or $u(\xi) = (h')^{-1}(x/t)$. Note that this solution only is unique when $h'(u)$ is a monotone increasing or decreasing function.

c) *Shock waves*. This is a discontinuity that fulfills Rankine-Hugoniot (3.6) with shock speed $\sigma = x/t$, and the Oleinik entropy condition (3.8) with strict inequalities. This solution is unique.

d) *Contact discontinuity*. This solution fulfills the same conditions as the shock waves, only with strict equality in Oleinik's entropy condition (3.8).

The solution of a Riemann problem is constructed by evaluating $h(u)$ between u^L and u^R. For $u^L < u^R$, the largest convex function that lies under $h(u)$ for $u \in [u^L, u^R]$ is identified (convex hull). Similarly, for the situation where $u^R < u^L$, the smallest concave function that lies over $h(u)$ for $u \in [u^R, u^L]$ is identified (concave hull). For a non-linear flux function $h(u)$, there are rarefaction waves where the hulls coincide with $h(u)$, and a discontinuity where the hulls is a chord. In the transition between a rarefaction wave and a shock, the shock velocity must be equal to $h'(u)$ in the transition point. For linear flux functions $h(u)$, the hulls will coincide with $h(u)$ and create contact discontinuities.

3.2.3 Properties

In Chapter 4, the non-linear scalar equation (3.4a) is discretized. To be better equipped to understand the properties of the discretized equation, some fundamental properties of the solution of scalar conservation laws in one dimension are given, following [43].

Theorem 1 *Let u_0 be an L^1-integrable function in x of bounded variation (real valued function with bounded total variation), and let $h(u)$ be a Lipschitz continuous function. Then, the weak entropy solution $u = u(x,t)$ to the initial value problem*

$$u_t + h(u)_x = 0, \qquad u(x,t) = u_0(x),$$

satisfies the following properties for all $t \in [0,\infty)$*:*

(i) ***Maximum principle****:*

$$||u(x,t)||_\infty \leq ||u_0||_\infty.$$

(ii) ***Total variation****: The total variation of a function* $u(x,t)$ *for a given* t *is*

$$TV(u) = \limsup_{\varepsilon \to 0} \frac{1}{\varepsilon} \int_{-\infty}^{\infty} |u(x+\varepsilon,t) - u(x,t)| \mathrm{d}x.$$

Note that if u *is continuously-differentiable, the total variation for a given* t *is*

$$TV(u) \int_{-\infty}^{\infty} |u'(x,t)| \mathrm{d}x.$$

(iii) L^1-***contractive****[58]: Let* v_0 *be an* L^1*-integrable function in* x *of bounded variation, and* $v = v(x,t)$ *is the entropy solution with* v_0 *as initial data. Then* u *and* v *are* L^1*-contracting, meaning that*

$$\textit{for all} \qquad t > 0, \qquad ||u(x,t) - v(x,t)||_1 \leq ||u(x,0) - v(x,0)||_1,$$

if and only if u *and* v *satisfy the Oleinik's entropy condition (3.8) at all shocks.*

(iv) ***Monotonicity****: Let* v_0 *be an* L^1*-integrable function in* x *of bounded variation, and* $v = v(x,t)$ *is the entropy solution with* v_0 *as initial data. Then*

$$u_0 \leq v_0 \qquad \textit{implies} \qquad u(x,t) \leq v(x,t),$$

for a given t*.*

(v) ***Monotinicity preservation****: If* u_0 *is monotone, this implies that* $u(x,t)$ *is monotone for a given* t*.*

Note that the indicated norms are defined as

$$||w(x)||_\infty = \sup_{x \in (-\infty,\infty)} |w(x)|, \qquad \text{and}$$

$$||w(x)||_1 = \int_{-\infty}^{\infty} |w(x)| \mathrm{d}x.$$

3.3 Spatially discontinuous flux function

Over the last decade, conservation laws with a spatial discontinuity in the flux function have gained attention. This is due both to their numerous applications and their intriguing theoretical challenges. The applications of these conservation laws include, i.e., heterogeneous two-phase flow [55] and traffic flow with discontinuous road surfaces [19]. In the previous section, entropy solutions for a conservation law with continuous

flux function were presented. The admissibility criteria are only valid for a flux function that depends smoothly on the spatial variable x. When a spatial discontinuity is present in the flux function, a new admissibility criterion across the discontinuity interface must be identified. The jump of the solution across the discontinuous interface of the flux function must satisfy this criterion. This topic has been discussed extensively in the literature, see, e.g., [1–3, 10, 20, 34, 35, 55, 62].

3.3.1 General framework

First, a spatial discontinuity in the flux function $h(u)$ of the scalar one-dimensional conservation law (3.4a) is introduced

$$h(u) = \begin{cases} h_L(u), & x < x_h, \\ h_R(u), & x \geq x_h, \end{cases} \tag{3.12}$$

where $u = u(x,t)$, h_L and h_R are Lipschitz continuous functions, and, to relate with the application of two-phase flow, let $u \in [0,1]$. Furthermore, it is assumed that $h_L(0) = h_R(0)$ and $h_L(1) = h_R(1)$ throughout this section. Now, $h(x,t)$ has a spatial dependence that is discontinuous at $x = x_h$ if the functions h_L and h_R are different. Using the Heaviside function $\overline{H}$

$$\overline{H}(x) = \begin{cases} 0, & x < 0, \\ 1, & x \geq 0, \end{cases}$$

the discontinuous flux function $h(u)$ can be written as

$$h(u) = \overline{H}(x - x_h) h_R(u) + \left(1 - \overline{H}(x - x_h)\right) h_L(u),$$

thus the scalar conservation law (3.4a) is

$$u_t + \left(\overline{H}(x - x_h) h_R(u) + \left(1 - \overline{H}(x - x_h)\right) h_L(u)\right)_x = 0. \tag{3.13}$$

Similarly to the continuous flux case presented in Section 3.2, a weak solution $u(x,t)$ of (3.4a) is found. That is, a bounded and measurable function u, such that for all test functions $\gamma(x,t) \in C_0^\infty(\overline{\mathbb{R} \times \mathbb{R}_+})$, the following equation is fulfilled:

$$\iint\limits_{\mathbb{R}\times\mathbb{R}_+} \left[u\gamma_t + \left(\overline{H}(x - x_h) h_R(u) + \left(1 - \overline{H}(x - x_h)\right) h_L(u)\right) \gamma_x\right] \, \mathrm{d}x\mathrm{d}t + \int\limits_{\mathbb{R}} u_0(x)\gamma(x,0) \, \mathrm{d}x = 0. \tag{3.14}$$

Away from the interface $x = x_h$, the theory presented in Section 3.2 is applied. To ensure that u is conserved through a shock at the interface $x = x_h$, any weak solution of (3.13) will satisfy the Rankine-Hugoniot condition for a zero-speed discontinuity

$$h_L(u^-(t)) = h_R(u^+(t)), \tag{3.15}$$

where $u^-(t)$ and $u^+(t)$ are called the left and right traces, respectively, and are defined by

$$u^-(t) = \lim_{x \to x_h^-} u(x,t), \qquad u^+(t) = \lim_{x \to x_h^+} u(x,t). \tag{3.16}$$

Before entropy conditions for this case are discussed, the framework of a spatial discontinuous flux function is connected to heterogeneous two-phase flow.

3.3.2 Entropy conditions

Similar to the continuous case, a weak solution is not necessarily unique. Entropy-conditions are imposed to ensure uniqueness and to ensure that the physically correct solution is chosen. Away from the discontinuity interface, $x = x_h$, the admissibility condition given by the Kružkov-type entropy condition (3.9) ensures well-posedness. In the literature, several different entropy conditions have been derived both from mathematical and physical considerations. We follow the framework of [2] and start by defining a connection called the $\{A,B\}$-*connection*.

Definition 6 ***{A,B}-connection***
If $h_L(u)$ and $h_R(u)$ have one global maximum and no local minimum for $u \in (0,1)]$, the maximum point of h_L and h_R will be denoted by θ_{h_L} and θ_{h_R}, respectively. Then $\{A,B\}$ is a connection if it satisfies

$$h_L(A) = h_R(B), \qquad \theta_{h_L} \leq A \leq 1 \qquad \text{and} \qquad 0 \leq B \leq \theta_{h_R}.$$

Similarly, if $h_L(u)$ and $h_R(u)$ have one global minimum and no local maximum for $u \in (0,1)$, the minimum point of h_L and h_R will be denoted by θ_{h_L} and θ_{h_R}, respectively. Then $\{A,B\}$ is a connection if it satisfies

$$h_L(A) = h_R(B), \qquad 0 \leq A \leq \theta_{h_L} \qquad \text{and} \qquad \theta_{h_R} \leq B \leq 1.$$

This means that A is in the region where $h_L(u)$ is decreasing, and B is in the region where $h_R(u)$ is increasing.

There are infinitely many $\{A,B\}$-connections to choose from, so some restrictions must be defined. First, assume that the traces (3.16) are defined for almost all t and let the *interface entropy functional* be defined as

$$I_{AB}(t) = \operatorname{sign}\left[u^-(t) - A\right]\left(h_L(u^-(t)) - h_L(A)\right) - \operatorname{sign}\left[u^+(t) + B\right]\left(h_R(u^+(t)) - h_R(B)\right).$$

For each connection $\{A,B\}$we have that the following *interface entropy condition* must hold

$$I_{AB}(t) \geq 0. \tag{3.17}$$

This condition is given as a definition in [2], but derived from the Kružkov-type entropy solution (3.9) in [20]. Now, the $\{A,B\}$-*entropy solution* can be defined.

Definition 7 ***{A,B}-entropy solution*** *A function $u \in L^\infty(\mathbb{R} \times \mathbb{R}_+)$ is defined as the entropy solution of (3.13) if the following holds*

(1) u is a weak solution of (3.13), i.e., u satisfies (3.14),

(2) u satisfies (3.9) away from the interface $x = x_h$, and

(3) u satisfies the interface entropy condition (3.17) relative to the $\{A,B\}$-connection.

For each choice of the $\{A,B\}$-connection, there is a different class of entropy solutions. In [2], and in the references therein, it is shown that for each choice of the $\{A,B\}$-connection there exists a unique AB-entropy solution.

In addition to the definitions of the $\{A,B\}$-connection given above, the connection must also be chosen according to the physical model the conservation law is representing. The classical approach to derive entropy conditions is to take the limit of higher order effects that can be modeled by dissipative, dispersive, and other higher order terms. These effects must reflect the physical model. The consideration of different higher order effects can lead to different solutions where each is reasonable with respect to the corresponding higher order effect. For the continuous case the vanishing viscosity limit is widely used. However, several theories have been proposed for choosing the $\{A,B\}$-connection when the flux function is discontinuous. For the heterogeneous two-phase flow application used in this work, the literature claims that the two most relevant theories are the *minimal variation condition* developed in [34, 35], and the *optimal entropy condition* from [2, 55]. These are the two conditions used throughout the included papers A and B.

In the framework of the vanishing viscosity limit, the *minimal jump condition* is considered to be the physically relevant condition, see e.g., [62],

Definition 8 ***Minimal jump condition***
Let A_m and B_m be chosen such that $|A_m - B_m|$ is minimized, this is the minimal jump condition.

The *optimal jump condition* originates from a vanishing capillary pressure limit. This condition is developed under the constraint that, in addition to continuity in flux over the interface (3.15), the pressure for each phase is continuous, hence the capillary pressure is also continuous. In [2], the *optimal jump condition* is given, equivalent to the theory developed in [55].

Definition 9 ***Optimal jump condition***
If h_L and h_R have one global maximum and no local minimum in $(0,1)$ and if $h_L(\theta_{h_L}) \geq h_R(\theta_{h_R})$, let $\theta^*_{h_R} \geq \theta_{h_L}$ such that $f^L(\theta^*_{h_R}) = h_R(\theta_{h_R})$. Similarly, if $h_L(\theta_{h_L}) < h_R(\theta_{h_R})$, let $\theta^*_{h_L} \leq \theta_{h_R}$ such that $h_R(\theta^*_{h_L}) = h_L(\theta_{h_L})$. Then, there exists a unique optimal connection $\{A_o,B_o\}$ given by

$$\{A_o,B_o\} = \begin{cases} \{\theta_{h_L},\theta^*_{h_L}\}, & \text{if } h_L(\theta_{h_L}) < h_R(\theta_{h_R}), \\ \{\theta^*_{h_R},\theta_{h_R}\}, & \text{if } h_L(\theta_{h_L}) \geq h_R(\theta_{h_R}). \end{cases} \tag{3.18a}$$

If h_L and h_R have one global minimum and no local maximum in $(0,1)$ and if $h_L(\theta_{h_L}) \geq h_R(\theta_{h_R})$, let $\theta^*_{h_L} \geq \theta_{h_R}$ such that $h_R(\theta^*_{h_L}) = h_L(\theta_{h_L})$. Similarly, if $h_L(\theta_{h_L}) < h_R(\theta_{h_R})$, let $\theta^*_{h_R} \leq \theta_{h_L}$ such that $h_L(\theta^*_{h_R}) = h_R(\theta_{h_R})$. Then, there exists a unique optimal connection $\{A_o,B_o\}$ given by

$$\{A_o,B_o\} = \begin{cases} \{\theta_{h_L},\theta^*_{h_L}\}, & \text{if } h_L(\theta_{h_L}) \geq h_R(\theta_{h_R}), \\ \{\theta^*_{h_R},\theta_{h_R}\}, & \text{if } h_L(\theta_{h_L}) < h_R(\theta_{h_R}). \end{cases} \tag{3.18b}$$

Note that in the case when $h_L(\theta_{h_L}) = h_R(\theta_{h_R})$ the optimal jump condition is $\{A_o,B_o\} = \{\theta_{h_L},\theta_{h_R}\}$.

To conclude this presentation of entropy conditions, a final remark about the characteristics at the interface $x = x_h$ in this system is made. Based on the form of the characteristics at the interface, the solution u is classified into the following classes:

(a) *Regular:* if either $h_L'(u^-(t)), h_R'(u^+(t)) \geq 0$ or $h_L'(u^-(t)), h_R'(u^+(t)) \leq 0$.

(b) *Overcompressive:* if $h_L'(u^-(t)) > 0$ and $h_R'(u^+(t)) < 0$.

(c) *Undercompressive:* if $h_L'(u^-(t)) < 0$ and $h_R'(u^+(t)) > 0$.

(d) *Marginally under(over)compressive:* if either $h_L'(u^-(t)) = 0$ and $h_R'(u^+(t)) \geq 0$, or $h_R'(u^+(t)) = 0$ and $h_L(u^-(t)) \leq 0$.

The optimal jump condition implies that the characteristics can not leave the discontinuity on both sides, this excluding the class of undercompressive waves. These characteristics can emerge from the interface and for these characteristics to be valid, a source of information must be present at $x = x_h$ for each characteristic line to be unique. Note that the minimal jump condition does not exclude these types of waves.

3.3.3 Riemann problem

In addition to having a discontinuous flux function, the initial data can be discontinuous as discussed for a continuous flux function in Section 3.2.2. This is also a Riemann problem, and for the situation with a discontinuous flux the problem reads

$$\begin{aligned} u_t + \left(\overline{H}(x-x_h)h_R(u) + \left(1-\overline{H}(x-x_h)\right)h_L(u)\right)_x &= 0, \\ u(x,0) &= \begin{cases} u^L, & \text{if} \quad x < 0, \\ u^R, & \textit{if} \quad x > 0. \end{cases} \end{aligned} \tag{3.19}$$

Away from the discontinuity interface $x = x_h$, the theory on this Riemann problem is equivalent to the case with a continuous flux function presented in Section 3.2.2. At the interface $x = x_h$, the entropy conditions for this Riemann problem were discussed in Section 3.3.2.

Example

The difference between the optimal and the minimal jump condition is best understood by looking at an example. Let the flux function be discontinuous across $x = 0$. In Figure 3.1a one classical example from [55] is shown where the two flux functions $h_L(u)$ and $h_R(u)$ cross in an undercompressive manner. That is $h_L'(u_c)$ and $h_R(u_c) > 0$, where u_x is the quantity where $h_L(u)$ and $h_R(u)$ intersects. This is a Riemann problem (3.19) with $u^L > u^R$. In this example the two flux functions h_L and h_R have one global minimum and no local maximum. According to definitions 8 and 9, the optimal and minimal jump conditions are given by

$$\{A_m, B_m\} = \{u_c, u_c\}, \qquad \text{and} \qquad \{A_o, B_o\} = \{\theta_{h_L}, \theta_{h_R}\}.$$

The interface entropy condition (3.17) combined with classical theory for solving the Riemann problem away from the discontinuity interface $x = 0$, for this example, gives different solution of the Riemann problem with the two jump conditions. Applying the minimal jump condition, the solution consists of a shock from u^L to u_c, followed

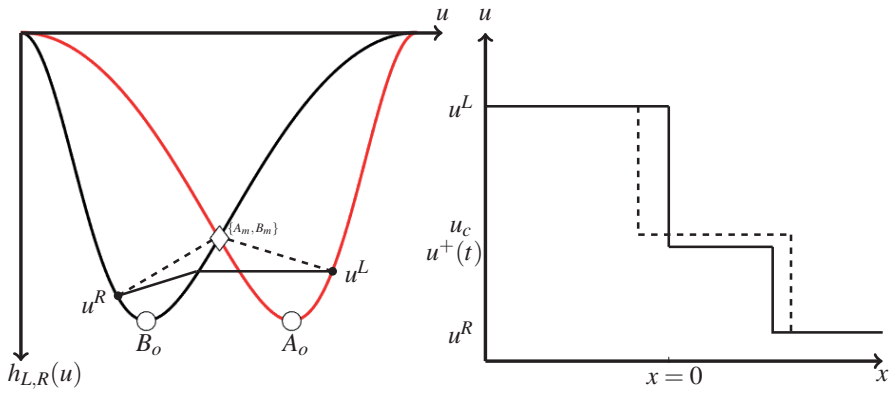

(a) Flux functions $h_L(u)$ and $h_R(u)$ in red and black, respectively. The minimal and optimal entropy solution are solid and dashed, respectively.

(b) Minimal (dashed) and optimal (solid) entropy solution.

Figure 3.1: Example of flux functions that cross in an undercompressive manner. Different entropy solutions using minimal and optimal jump condition.

by a shock from u_c to u^R. Applying the optimal jump condition the solution is a constant state from u^L to $u^+(t)$ followed by a shock to u^R. In Figure 3.1b the solutions corresponding to the minimal and optimal jump conditions are given.

3.3.4 Heterogeneous two-phase flow

In most realistic applications, the porous medium is heterogeneous and the flow domain can be divided into several subdomains corresponding to different types of rock. Consider the one-dimensional scalar equation of two-phase flow (2.14). Let the porous medium be heterogeneous and the interface at which the rock changes be denoted by $x = x_h$. This introduces a spatial discontinuity in the flux function f through the permeabilities (and possibly the porosity), and the flux function is given by

$$f(s) = \begin{cases} f^L(s) = \frac{\lambda_w^L}{\lambda_w^L + \lambda_n^L}\left(v + \lambda_n^L (g_w - g_n)\right), & x < x_h, \\ f^R(s) = \frac{\lambda_w^R}{\lambda_w^R + \lambda_n^R}\left(v + \lambda_n^R (g_w - g_n)\right), & x \geq x_h, \end{cases}$$

where s represents the saturation of the wetting phase $s = s_w$, and λ_α^L and λ_α^R are the mobilities to the left and right of the discontinuity, respectively. These are given by

$$\lambda_\alpha^L = K^L \frac{k_{r\alpha}^L}{\mu_\alpha}, \qquad \text{and} \qquad \lambda_\alpha^R = K^R \frac{k_{r\alpha}^R}{\mu_\alpha},$$

where K^L, K^R and $k_{r\alpha}^L, k_{r\alpha}^R$ represent absolute and relative permeabilities to the left and to the right of the interface $x = x_h$.

Remark

Recently, a new and ongoing discussion regarding what is considered to be the physically relevant entropy condition has developed in the literature. In [55] it is shown that the solution originating from the optimal entropy connection coincides with the so called *vanishing capillarity solution*, which is considered to be the physically relevant solution. The solution using the optimal $\{A,B\}$-connection is also considered to be the physically relevant one in other works on this topic, see e.g., [2] and the references therein. However, this conclusion was discussed and shown to be erroneous in the recent works [8, 9].

The homogeneous one-dimensional Buckley-Leverett equation for incompressible flow, (2.14), without neglecting capillary pressure, is given by

$$\begin{aligned} \phi s_t + f(s)_x = & \left(\bar{\lambda}\left[P_C\right]_x\right)_x, \\ f(s) = & \frac{\lambda_w}{\lambda_w + \lambda_n}\left(v + \lambda_n\left(\left(g_w - g_n\right)\right)\right), \end{aligned}$$

where $\bar{\lambda} = \frac{\lambda_w \lambda_n}{\lambda_w + \lambda_n}$, and $g_\alpha = \rho_\alpha g \cos(\theta)$ and $\alpha = w,n$, is the influence of gravity at the angle θ from the vertical axis. In many homogeneous applications it is common to neglect the diffusive term involving the capillary pressure P_C. The reasoning for this is that the time and space scales considered for observing the dynamic of the flow are much larger than the scales where diffusion may have an effect. Let $t = t/\varepsilon$ and $x = x/\varepsilon$, where $\varepsilon > 0$ is a small parameter. This substitution leads to

$$\phi\left(s^\varepsilon\right)_t + \left(f(s^\varepsilon)\right)_x = \varepsilon\left(\bar{\lambda}\left[P_C\right]_x\right)_x. \tag{3.20}$$

The vanishing capillarity *model* is obtained by taking the limit $\varepsilon \to 0$ of the model (3.20). The vanishing capillarity *limit* is the solution of this model, and is the vanishing capillarity *solution*. This is considered to be the physically relevant solution, but is not necessarily a unique solution. To select the unique vanishing capillarity solution, the Kružkov entropy condition (3.9) is applied to the homogeneous case. This condition is independent of the capillary pressure and capillarity forces can be fully neglected. Note that this criterion was first introduced in the so called *vanishing viscosity* framework for the Burgers equation. However, it turned out that this was equivalent to the vanishing capillary limit for two-phase flow in homogeneous rock.

The case of heterogeneous rock is more complicated than the homogeneous one. Let the interface between the two rocks be located at $x = 0$. In [9] it is emphasized that

even if the macroscopic capillary pressure is neglected, the capillary forces play a major role at the interface between different rocks. Thus, capturing the singular effect at the interface may be necessary to find the physically relevant solution. In [8, 9] it is shown that full knowledge of the capillary pressure curve is necessary to identify the vanishing capillarity solution.

To capture the effect from the capillary force at the interface, one has to allow the interface to generate information. This means that some undercompressive discontinuities should be allowed at $x = 0$. This contradicts the use of the Lax criterion used in [55] and the interpretation of the optimal entropy condition (which excludes these discontinuities) as the correct one. Furthermore, the theory developed in [55] is based on the assumption that the case that both $f^L(s^-(t)) = f^R(s^+(t))$ and $P_C^L(s^-(t)) = P_C^R(s^+(t))$ are considered to be "merely coincidental". However, this is not in general a valid assumption.

3.4 A system of conservation laws modeling polymer flooding

Returning to a hyperbolic conservation law where the flux function is continuous, and unlike in Section 3.2, a *system* of conservation laws is now considered. The corresponding Riemann problem is more challenging to solve. In the following, the application of polymer flooding presented in Section 2.2.2 is discussed in this context. The theory presented herein follows the framework of [51] and [4].

For clarity of exposition, the system of conservation laws modeling polymer flooding (2.19) is rewritten below

$$\begin{aligned} s_t + f(s,c)_x &= 0, \\ (sc + a(c))_t + cf(s,c)_x &= 0, \end{aligned} \tag{3.21}$$

where $s = s_w$ and the flux function $f(s,c)$ is given by

$$f(s,c) = \frac{\lambda_w}{\lambda_w + \lambda_n}\left(v \pm \lambda_n(g_w - g_n)\right). \tag{3.22}$$

By expanding the derivatives in the equations (3.21), the following non-conservative system of equations is obtained

$$\begin{aligned} s_t + f_s(s,c)s_x + f_c(s,c)c_x &= 0, \\ (s + a'(c))c_t + f(s,c)c_x &= 0. \end{aligned} \tag{3.23}$$

The system (3.23) can be written in the matrix form

$$\tilde{U}_t + A(\tilde{U})\tilde{U}_x = 0,$$

where $\tilde{U}$ denotes the state vector $\tilde{U} = [s\ c]$, and the Jacobian matrix $A(\tilde{U})$ is given by

$$A(\tilde{U}) = \begin{bmatrix} f_s & f_c \\ 0 & \frac{f}{s+a'(c)} \end{bmatrix}.$$

The eigenvalues λ^i of A are given by

$$\lambda^s = f(s,c)_s, \qquad \text{and} \qquad \lambda^c = \frac{f(s,c)}{s+a'(c)}.$$

The corresponding eigenvectors are given by $E^s = [1,0]$ and $E^c = [f_c, \lambda^c - \lambda^s]$ if $s \in (0,1)$,and $E^c = [0,1]$ if $s = 0,\ 1$. Note that λ^s can change sign, whilst λ^c is always positive. For each $c \in [0,1]$ there exists a unique $s^T = s^T(c)$ such that

$$\lambda^s(s^T,c) = \lambda^c(s^T,c),$$

hence the eigenvectors are not linearly independent and the problem is non-strictly hyperbolic.

3.4.1 Discontinous solutions

When $c^L \neq c^R$, any weak solution of (3.21) needs to satisfy the Rankine-Hugoniot jump condition

$$f(s^R,c^R) - f(s^L,c^L) = \sigma(s^R - s^L), \tag{3.24a}$$
$$c^R f(s^R,c^R) - c^L f(s^L,c^L) = \sigma(s^R c^R + a(c^R) - s^L c^L - a(c^L)). \tag{3.24b}$$

By combining (3.24a) and (3.24b),

$$(c^R - c^L) f(s^L,c^L) = \sigma(c^R - c^L)s^L + \sigma(a(c^R) - a(c^L)),$$

is obtained, where

$$\sigma = \frac{f(s^L,c)}{s^L + \tilde{a}(c^R)}, \qquad \text{and} \qquad \tilde{a}(c) = \begin{cases} \frac{a(c)-a(c^L)}{c-c^L}, & \text{if} \quad c \neq c^L, \\ a'(c), & \text{if} \quad c = c^L. \end{cases}$$

By inserting this into (3.24a),

$$\sigma(s^R + \tilde{a}(c^R)) = \sigma\left(s^L + \tilde{a}(c^R)\right) + f(s^R,c^R) - f(s^L,c^L) = f(s^R,c^R),$$

is obtained. Hence, when $c^L \neq c^R$, the Rankine-Hugoniot condition (3.24a)-(3.24b) reduces to

$$\frac{f(s^R,c^R)}{s^R + \tilde{a}(c^R)} = \frac{f(s^L,c^L)}{s^L + \tilde{a}(c^R)} = \sigma. \tag{3.25}$$

To find the physically meaningful weak solution of (3.21), it is required that a shock wave is evolutionary, details of which may be found in, e.g., [51].

3.4.2 Riemann problem

In the industry, polymers are often injected as slugs, creating discontinuities. Therefore, discontinuous initial data needs to be considered. The system (3.21), combined with the initial conditions

$$s(x,0) = \begin{cases} s^L, & \text{if } x < 0, \\ s^R, & \text{if } x \geq 0, \end{cases} \qquad c(x,0) = \begin{cases} c^L, & \text{if } x < 0, \\ c^R, & \text{if } x \geq 0, \end{cases} \tag{3.26}$$

is a Riemann problem. This problem (with the adsorption $a(c) = 0$) was first analyzed by [47, 85], who neglected gravity and studied a system in which the flux function $f(s,c)$ is monotone. The extension of this model with $a(c) \neq 0$ was analyzed in [51] and a unique global solution of this Riemann problem was derived. When gravity effects are included, the flux function can be non-monotone and the eigenvalues λ^p can change sign. Thus, the exact solution of the Riemann problem is more difficult to construct. General Riemann problems for this system are considered in [4, 84]. Following [4], the main theory of the related solution strategy is provided below.

First, some assumptions on the flux function $f(s,c)$ and the adsorption term $a(c)$ are given:

- $f(0,c) = 0$ for all $c \in [0,1]$,
- $f(1,c) = constant$ for all $c \in [0,1]$,
- $f_c(s,c) < 0$ for all $s \in (0,1)$ and for all $c \in [0,1]$,
- $a(0) = 0$, $a'(c) > 0$, and $a''(c) < 0$.

The solution of the general Riemann problem consists of what in the literature is referred to as s-waves and c-waves. An s-wave is any composition of simple rarefaction or shock (or contact discontinuity) waves across which s changes continuously and discontinuously, respectively, whilst c remains constant. These waves correspond to the wave of a scalar Riemann problem, presented in Section 3.2.2. A c-wave is a simple c-rarefaction wave or a c-shock (or contact discontinuity) such that s and c change but $\frac{f(s,c)}{s+a'(c)}$ remains constant.

A closer look at the solution of the Riemann problem will be given for the case in which $c^L > c^R$, as well as the case where the flux functions $f(s,c^L)$ and $f(s,c^R)$ have one global maximum and no local minimum in $(0,1)$, i.e., the concave type. Thus, some additional assumptions have been made for the flux function $f(s,c)$:

- The function $s \to f(s,c)$ has exactly one global maximum for $s \in [0,1]$, and no other local minimum,
- $f(1,c) = 0$ for all $c \in [0,1]$.

Thus, advection v in the flux function (3.22) is neglected for now. However, the solution of the Riemann problem presented below can be extended to include advection straight forward. Note that since $c^L > c^R$, $f(s,c^L) \leq f(s,c^R)$ for $\forall s \in (0,1)$. The presentation follows the one given in [4] and the solution of the Riemann problem is divided into four sub cases. To present these cases, let the line through $(-\tilde{a}(c^R),0)$ and $(s^T, f(s^T,c^L))$

intersect the curve $f(s,c^R)$ at the point $(s^A, f(s^A,c^R))$ where $f_s(s,c^R) < 0$, see Figure 3.2a-d. Furthermore, let the line through $(-\tilde{a}(c^R),0)$ and $(s^L, f(s^L,c^L))$ intersect the curve $f(s,c^R)$ at the point $(s^B, f(s^B,c^R))$, where $f_s(s,c^R) < 0$, see Figure 3.2a-d. Now, the solution of the Riemann problem is separated by the four sub-cases:

a) $s^L < s^T$ and $s^R < s^B$, illustrated in Figure 3.2a.

First the state (s^L,c^L) is connected to the intermediate state (s^M,c^R) by a c-wave with speed

$$\sigma_c = \frac{f(s^L,c^L)}{s^L+\tilde{a}(c^R)} = \frac{f(s^M,c^R)}{s^M+\tilde{a}(c^R)}.$$

Next, the state (s^M,c^R) is connected to (s^R,c^R) by an s-wave along the curve $f(s,c^R)$.
For the specific case in Figure 3.2a where $s^R > s^M$, the solution of the Riemann problem is given by

$$(s(x,t),c(x,t)) = \begin{cases} (s^L,c^L), & \text{if} \quad x < \sigma_c t, \\ (s^M,c^R), & \text{if} \quad \sigma_c t < x < \sigma_s t, \\ (s^R,c^R), & \text{if} \quad x > \sigma_s t, \end{cases} \tag{3.27a}$$

where σ_c is given above, and

$$\sigma_s = \frac{f(s^M,c^R) - f(s^R,c^R)}{s^M - s^R}.$$

The corresponding characteristics are shown in Figure 3.3a.

b) $s^L < s^T$ and $s^R \geq s^B$, illustrated in Figure 3.2b,

First, the state (s^L,c^L) is connected to the intermediate state (s^M,c^L) by an s-wave along the curve $f(s,c^L)$.
Next, the state (s^M,c^L) is connected to (s^R,c^R) by a c-wave with the speed

$$\sigma_c = \frac{f(s^R,c^R)}{s^R+\tilde{a}(c^R)} = \frac{f(s^M,c^L)}{s^M+\tilde{a}(c^R)}.$$

For the specific case shown in Figure 3.2b, the solution of the Riemann problem is given by

$$(s(x,t),c(x,t)) = \begin{cases} (s^L,c^L), & \text{if} \quad x < \sigma_s t, \\ (s^M,c^L), & \text{if} \quad \sigma_s t < x < \sigma_c t, \\ (s^R,c^R), & \text{if} \quad x > \sigma_c t, \end{cases} \tag{3.27b}$$

where σ_c is defined above and

$$\sigma_s = \frac{f(s^M,c^L) - f(s^L,c^L)}{s^M - s^L}.$$

The corresponding characteristics are shown in Figure 3.3b.

c) $s^L \geq s^T$ and $s^R \leq s^A$, illustrated in Figure 3.2c.

First, connect the state (s^L, c^L) to the intermediate state (s^T, c^L) by an s-wave along the curve $f(s, c^L)$.
Next, connect the state (s^T, c^L) to the second intermediate state (s^M, c^R) by a c-wave, where

$$\sigma_c = \frac{f(s^T, c^L)}{s^M + \tilde{a}(c^R)}.$$

Finally, connect the state (s^M, c^R) to the state (s^R, c^R) by an s-wave along the curve $f(s, c^R)$.
For the specific case shown in Figure 3.2c, where $s^R < s^M$, the solution of the Riemann problem is given by

$$(s(x,t), c(x,t)) = \begin{cases} (s^L, c^L), & \text{if} \quad x < \sigma_{s1} t, \\ ((f_s)^{(-1)}(\frac{x}{t}, c^L), c^L), & \text{if} \quad \sigma_{s1} t < x < \sigma_c t, \\ (s^M, c^R), & \text{if} \quad \sigma_c t < x < \sigma_{s2} t, \\ ((f_s)^{(-1)}(\frac{x}{t}, c^R), c^R), & \text{if} \quad \sigma_{s2} t < x < \sigma_{s3} t, \\ (s^R, c^R), & \text{if} \quad x > \sigma_{s3} t, \end{cases} \tag{3.27c}$$

where σ_c is defined above, and

$$\sigma_{s1} = f_s(s^L, c^L), \qquad \sigma_{s2} = f_s(s^M, c^R), \qquad \text{and} \qquad \sigma_{s3} = f_s(s^R, c^R).$$

Note that both s-waves in this case are rarefaction waves. If $s^R > s^M$ the second s-wave would be a shock. The corresponding characteristics are shown in Figure 3.3c.

d) $s^L \geq s^T$ and $s^R > s^A$, illustarted in Figure 3.2d.

First, the state (s^L, c^L) is connected to the intermediate state (s^M, c^L) by an s-wave along the curve $f(s, c^L)$.
next, the state (s^M, c^L) is connected to the state (s^R, c^R) by a c-wave with speed

$$\sigma_c = \frac{f(s^R, c^R)}{s^R + \tilde{a}(c^R)} = \frac{f(s^M, c^L)}{s^M + \tilde{a}(c^R)}.$$

For the specific case shown in Figure 3.2d, where $s^L < s^M$, the solution to the Riemann problem is given by

$$(s(x,t), c(x,t)) = \begin{cases} (s^L, c^L), & \text{if} \quad x < \sigma_s t, \\ (s^M, c^L), & \text{if} \quad \sigma_s t < x < \sigma_c t, \\ (s^R, c^R), & \text{if} \quad x > \sigma_c t, \end{cases} \tag{3.27d}$$

where σ_c is defined above, and

$$\sigma_s = \frac{f(s^M, c^L) - f(s^L, c^L)}{s^M - s^L}.$$

The corresponding characteristics are shown in Figure 3.3d.

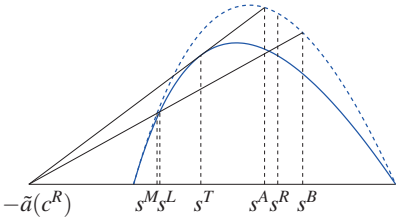

(a)

Case a), where $s^L < s^T$ and $s^R < s^B$.

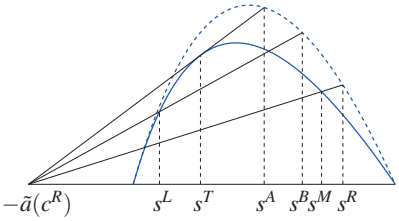

(b)

Case b), where $s^L < s^T$ and $s^R \geq s^B$.

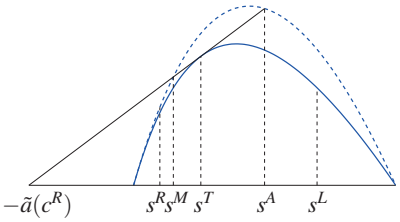

(c)

Case c), where $s^L \geq s^T$ and $s^R \leq s^A$.

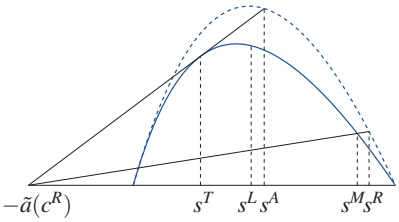

(d)

Case d), where $s^L \geq s^T$ and $s^R > s^A$.

Figure 3.2: Illustration of the four sub cases a-d described above. Note that $c^L > c^R$ and the flux function $f(s, c^L)$ is shown in blue whilst the flux function $f(s, c^R)$ is given in dashed blue. What separates the four cases are the values s^L and s^R.

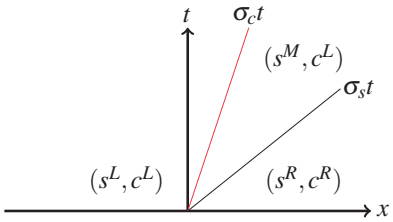

(a)

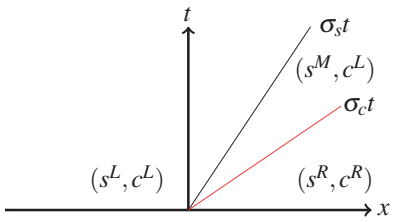

(b)

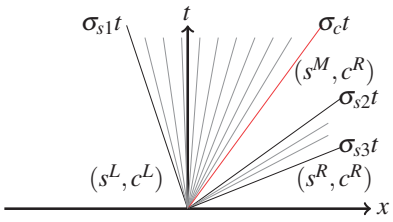

(c)

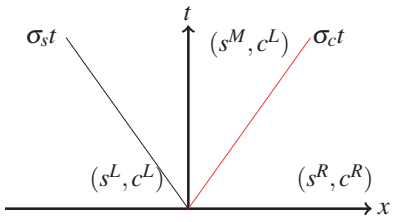

(d)

Figure 3.3: Characteristics in the xt-plane corresponding to the four cases illustrated in Figure 3.2. Note that the characteristics representing c-waves is given in red.

The case where $c^R > c^L$ must be analyzed with similar sub-cases. Likewise, for convex flux functions, see, e.g., [84]. Note that [51] analyzed the cases $c^L > c^R$ and $c^L < c^R$ for a monotone flux function. However, the presentation in [51] is based on the location of the states (s^L, c^L) and (s^R, c^R) with respect to the transition curve $\mathcal{T}$, in the sc-plane, given by

$$\mathcal{T} = \{(s,c) | \lambda^s(s,c) = \lambda^c(s,t)\}.$$

This approach results in the same sub-cases as discussed in this presentation.

Chapter 4

Numerical framework

To solve the hyperbolic conservation laws discussed so far, a numerical framework must be introduced. The domain of the equation is discretized and a conservative numerical scheme is introduced. Important properties of numerical schemes in general are discussed, before some specific schemes and their properties for non-linear hyperbolic PDEs are introduced. To conclude this chapter, the specific numerical framework of the applications discussed in the included papers is given. The general references on numerical methods for hyperbolic conservation laws used throughout this chapter are [66, 67, 87, 88].

4.1 Discretization

Numerical methods replace the continuous problem represented by a partial differential equation, e.g., (3.3),

$$U_t + H(U)_x = 0,$$

by a finite set of discrete values. To obtain these discrete values, the domain of the equation is discretized through a *mesh* or a *grid* into a finite set of points or volumes.

The spatial domain is subdivided into a finite number of finite volumes, called *cells*. The size of each cell i is Δx_i. The temporal domain is also subdivided into subdomains with time step Δt. The discrete grid points (x_i, t^n) are defined by

$$\begin{aligned} x_i &= i\Delta x_i, \qquad i = \cdots, -1, 0, 1, \cdots, \\ t^n &= n\Delta t, \qquad n = 0, 1, 2, \cdots. \end{aligned}$$

Note that x_i represents the cell-centers, whilst $x_{i\pm 1/2}$ represents the edges of the cell

$$x_{i\pm 1/2} = x_i \pm \frac{\Delta x}{2} = \left(i \pm \frac{1}{2}\right)\Delta x_i,$$

as illustrated in Figure 4.1. For the applications used in this work, the width of each cell Δx_i is taken to be constant, or *equidistant*, across the domain.

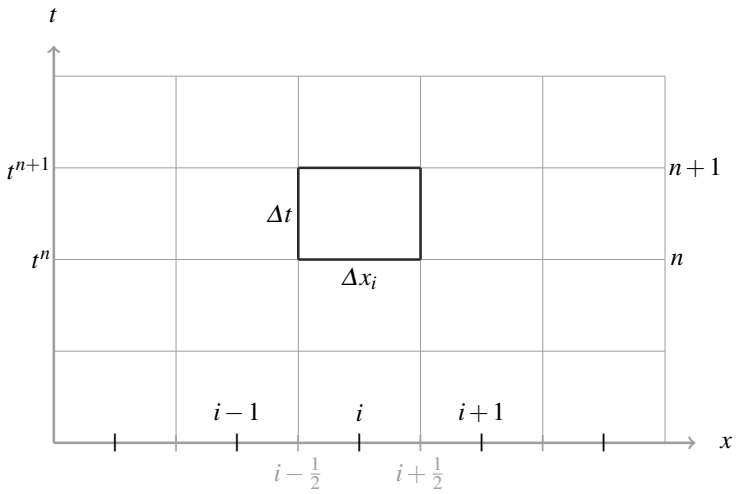

Figure 4.1: Discretization of the xt-plane.

In the *finite difference* approach, the approximation or discrete values U_i^n are considered as *point-values* defined by the grid point,

$$U_i^n = U(x_i, t^n). \tag{4.1}$$

For the *finite volume* approach, these discrete values are *averages over finite volumes*. If the domain Ω is divided into a set of finite sub-domains Ω_i, the *cell average* $\bar{U}_i^n$ of U over each grid cell Ω_i in one spatial dimension is given by

$$\bar{U}_i^n = \frac{1}{\Delta x} \int_{x_{i-1/2}}^{x_{i+1/2}} U(x, t^n)\, \mathrm{d}x. \tag{4.2}$$

It is often preferable to view U_i^n as an approximation to cell averages (4.2) instead of an approximation to point-values (4.1), especially when developing methods for conservation laws. For this reason, the focus in this presentation will be from the finite-volume approach and the notation U_i^n from now on represents the cell average defined in (4.2).

4.1.1 Conservative schemes

To motivate the numerical schemes, the integral form of the conservation law (3.1) is imposed on the grid cell $\Omega_i = [x_{i-1/2}, x_{i+1/2}]$. This is combined with the divergence theorem and the fundamental theorem of calculus to obtain

$$\frac{d}{dt} \int_{x_{i-1/2}}^{x_{i+1/2}} U(x,t)\, \mathrm{d}x = H(U(x_{i-1/2}, t)) - H(U(x_{i+1/2}, t)). \tag{4.3}$$

Integrating this in time over the interval $[t^n, t^{n+1}]$ results in

$$\int_{x_{i-1/2}}^{x_{i+1/2}} U(x,t^{n+1})\,\mathrm{d}x - \int_{x_{i-1/2}}^{x_{i+1/2}} U(x,t^n)\,\mathrm{d}x = \int_{t^n}^{t^{n+1}} H(U(x_{i-1/2},t))\,\mathrm{d}t - \int_{t^n}^{t^{n+1}} H(U(x_{i+1/2},t))\,\mathrm{d}t.$$

Rearranging and dividing by Δx_i gives

$$\frac{1}{\Delta x_i}\int_{x_{i-1/2}}^{x_{i+1/2}} U(x,t^{n+1})\,\mathrm{d}x = \frac{1}{\Delta x_i}\int_{x_{i-1/2}}^{x_{i+1/2}} U(x,t^n)\,\mathrm{d}x - \frac{1}{\Delta x_i}\left[\int_{t^n}^{t^{n+1}} H(U(x_{i+1/2},t))\,\mathrm{d}t - \int_{t^n}^{t^{n+1}} H(U(x_{i-1/2},t))\,\mathrm{d}t\right].$$

Here, $U(x_{i\pm1/2},t)$ varies with time along each cell edge and we cannot evaluate the integrals exactly. However, this motivates us to study schemes in the *conservation form*:

$$U_i^{n+1} = U_i^n - \frac{\Delta t}{\Delta x_i}\left(\tilde{H}_{i+1/2} - \tilde{H}_{i-1/2}\right), \tag{4.4}$$

where $\tilde{H}_{i\pm1/2}$ is called the numerical flux at the cell edge $x_{i\pm1/2}$, and represents an approximation to the average flux $H(U)$ over each cell edge $x = x_{i\pm1/2}$:

$$\tilde{H}_{i\pm1/2} \sim \frac{1}{\Delta t}\int_{t^n}^{t^{n+1}} H(U(x_{i\pm1/2},t))\,\mathrm{d}t. \tag{4.5}$$

Since the information in a hyperbolic problem propagates with a finite speed, it is natural to assume that the numerical flux across the cell edge $x = x_{i+1/2}$ depends on the cell averages U_i^n and U_{i+1}^n on the left and the right side of the edge, respectively. That is,

$$\tilde{H}_{i+1/2} = \tilde{H}(U_i^n, U_{i+1}^n).$$

This means that the numerical scheme is *explicit* since the flux is approximated using values of U at time t^n. In an *implicit* scheme the flux is approximated using values of U at time t^{n+1}.

The values U_i^n and U_i^{n+1} are cell averages of U, and the cell averages need to be reconstructed to represent point-values to be used in the approximation of the flux. The simplest reconstruction function $\tilde{U}(x,t^n)$ is a piecewise constant function that takes the value U_i^n in the i-th grid cell

$$\tilde{U}(x,t^n) = U_i^n. \tag{4.6}$$

Note that the average value of the reconstruction $\tilde{U}_i^n$ over the cell $[x_{i-1/2}, x_{i+1/2}]$ is U_i^n.

To summarize, different numerical schemes are separated by how the flux across the cell edge (4.5) are approximated, and how the the reconstruction function $\tilde{U}(x,t^n)$ is defined. For now, the piecewise constant reconstruction (4.6) is used and other reconstructions will be presentd in Section 4.4.

4.1.2 Semi-discrete equations

Sometimes it is useful to do the discretization process in two stages. First, a discretizing in space is done, leading to a system of ordinary differential equations in time, called the *semi-discrete equations*. Next, the discretization in time is done using a standard numerical method for systems of ordinary differential equations.

To derive the semi-discrete equations for the evolution of cell averages U_i^n at time $t = t^n$, Equation (4.3) is combined with the expression for the cell average (4.2). Thus, we arrive at the following system of ODEs:

$$\frac{d}{dt}U_i^n = -\frac{1}{\Delta x}\left(\tilde{H}_{i-1/2} - \tilde{H}_{i+1/2}\right), \tag{4.7}$$

where $\tilde{H}_{i\pm1/2}$ again represents numerical approximations to the flux across the cell edges (4.5).

4.2 Properties

A numerical scheme is said to be convergent if the numerical solution converges to the true solution of the differential equation as the grid is refined ($\Delta x_i, \Delta t \to 0$). It is important to determine whether a numerical scheme is expected to converge, and whether it converges to the correct solution. However, for real problems the true solution is generally not known. To have some notion of whether a numerical scheme converges, several properties of a numerical scheme are defined throughout this section.

A numerical scheme in conservation form (4.4) is based on the integral form of the conservation law. This guarantees that the discrete solution will be conservative. Furthermore, any numerical scheme must be *consistent* with the differential equation it is approximating. This means that it approximates the differential equation well, locally. The numerical flux approximation is designed to approximate (4.5), and in particular if $U(x,t)$ is constant, $U(x,t) = \bar{U}$, then U will not change in time. Thus, as a part of the requirement to be consistent, the integral (4.5) reduces to $H(\bar{U})$, and

$$\tilde{H}(U_i^n, U_i^{n+1}) = H(\bar{U}).$$

Furthermore, when $U_i^n \neq U_{i+1}^n$ it is required that $H(U_i^n, U_i^{n+1})$ is Lipschitz continuous. This means that there exists a constant C such that

$$|\tilde{H}(V,W) - H(U)| \leq C\max(|V-U|, |W-U|),$$

for all V, W with $|V-U|$ and $|W-U|$ sufficiently small.

Lax and Wendroff [64] proved that if the discrete solution converges to some function $U(x,t)$ as the grid is refined, $\Delta x_i \to 0, \Delta t \to 0$, then this function will be a weak solution of the conservation law.

Theorem 2 ***Lax-Wendroff theorem***
Consider a sequence of grids indexed by $i = 1,2,\cdots$ with $\Delta t^{(j)}, \Delta x_i^{(j)} \to 0$ as $j \to \infty$. Let $U^{(j)}(x,t)$ denote the numerical approximation computed by a conservative and consistent scheme on the j-th grid. Suppose that $U^{(j)}$ converges to a function U as $j \to \infty$. Then $U(x,t)$ is a weak solution of the conservation laws.

In practice only a single approximation on a fixed grid is computed. If this solution looks reasonable and has well-resolved discontinuities, then one can believe that this approximation is a good approximation to some weak solution [67]. Note that the Lax-Wendroff theorem is valid both for scalar conservation laws as well as systems of conservation laws.

However, the Lax-Wendroff theorem does not guarantee that convergence occurs. For that, some form of stability is necessary. A numerical scheme must be stable so that small errors made in each time step do not grow too fast in later time steps. A detailed discussion on stability theory for non-linear schemes will not be given here. However, a *necessary* condition for stability of any finite volume or finite difference scheme is known as the *CFL condition* named after Courant, Friedrichs, and Lewy who wrote one of the first papers on finite difference methods [26]. This condition says that the domain of dependence of the exact solution, which is bounded by the characteristics of the largest and smallest eigenvalues of the Jacobian matrix $H'(U)$, should be contained in the domain of dependence for the discrete equation. For a three-point numerical stencil in which U_i^{n+1} depends on U_{i-1}^n, U_i^n, and U_{i+1}^n, the CFL condition is given by

$$\frac{\Delta t}{\Delta x} \max_{i,p} |\lambda^p(U_i)| \leq 1,$$

where $\lambda^p(U_i)$ are the p eigenvalues of the Jacobian matrix of the flux function H. If the method has a wider stencil, e.g., a centered five-point stencil in which U_i^{n+1} also depends on U_{i-2}^n and U_{i+2}^n, the CFL condition is given by

$$\frac{\Delta t}{\Delta x} \max_{i,p} |\lambda^p(U_i)| \leq 2.$$

The CFL condition is not a sufficient criteria for stability. For linear problems, the *Lax-Richtmeyer* stability theory guarantees convergence. For the non-linear case, stability can be obtained by requiring monotonicity. A scheme is said to be monotone if

$$\frac{\partial U_i^{n+1}}{\partial U_j^n} \geq 0 \qquad \forall i, j.$$

This means that if the value U_j^n at time t^n is increased, then the value U_i^{n+1} at the next time step cannot decrease. A monotone scheme cannot generate spurious oscillations in the approximated solution. To require monotonicity will be sufficient to guarantee convergence to the correct entropy solution. Unfortunately, the monotonicity property only holds for certain first-order accurate schemes.

To measure oscillations in the solution, the total variation of a discrete function U_i^n is introduced:

$$\mathrm{TV}(U^n) = \sum_{\forall i} |U_i^n - U_{i-1}^n|.$$

If the numerical scheme introduces oscillations, the total variation of the discrete function would expect to increase with time. Based on this, it is shown in [39] that oscillations for a scalar hyperbolic equation can be avoided by requiring that the scheme does not increase the total variation.

Definition 10 ***Total variation diminishing***
A numerical scheme is called total variation diminishing (TVD) if, for any set of data U^n, the values U^{n+1} computed by the scheme satisfy

$$TV(U^{n+1}) \leq TV(U^n). \tag{4.8}$$

The total variation does not need to be diminishing in the sense of decreasing, it can remain constant in time. If a scheme is TVD and the data is initially monotone, the data will remain monotone in all future time steps. Hence, if a single propagating discontinuity is discretized, the discontinuity can be smeared, but not become oscillatory in future time steps. It can be shown that any TVD scheme is monotonicity-preserving, but the converse is not necessarily true. Note that the TVD property only ensures an oscillation free solution for scalar equations. Since we want the numerical scheme to mimic known properties for the scalar conservation law, see Section 3.2.3, the hope is that the property of having a TVD numerical scheme also is beneficial for systems. To complete this short introduction on TVD schemes, Harten's result from [39] is presented:

Theorem 3 ***Harten's theorem***
Consider a numerical scheme of the form

$$U_i^{n+1} = U_i^n - C_{i-1}^n(U_i^n - U_{i-1}^n) + D_i^n(U_{i+1}^n - U_i^n),$$

over one time step, where the coefficients C_{i-1}^n and D_i^n can depend on values of U^n in some way. Then the scheme is TVD provided that:

$$C_{i-1}^n \geq 0, \qquad D_i^n \geq 0, \qquad \textit{and} \qquad C_i^n + D_i^n \leq 1, \qquad \forall i.$$

The error in each step of a numerical solution is called the local truncation error, while the total error for the whole interval is called the global truncation error. The order of any scheme is said to be the power of Δx_i in the global truncation error. Thus, schemes with global truncation error $\mathrm{O}(\Delta x_i)$ in smooth parts of the solution are first-order schemes.

To discuss the convergence of a numerical solution for a scalar conservation law further the piecewise-constant function $U^{(\Delta x_i, \Delta t)}(x,t)$ is defined

$$U^{(\Delta x_i, \Delta t)}(x,t) = U_i^n \qquad \text{for } (x,t) \in [x_{i-1/2}, x_{i+1/2}) \times [t^n, t^{n+1}],$$

where the index $(\Delta x_i, \Delta t)$ denotes that the numerical solution depends on the particular grid that is used.

Efficiency of a numerical method is often measured by comparing the computational time required to achieve a specified numerical *accuracy*. To measure accuracy we recognize that the numerical solution is defined as point-values or cell averages on the grid, while the true solution of the PDE is defined on an interval in space. To overcome this, the numerical solution can be extended to all of the problem domain and then applying standard norms. Typically, due to the properties of the solution of the scalar equation, the L^1 norm is used in this comparison [88]. Since the numerical solution values are taken to be approximations of the cell averages of the solution, it seems reasonable to define an average of the function $U(x,t^n)$ over a cell $(x_{i-1/2}, x_{i+1/2})$ by

$$A(U) = \frac{1}{x_{i+1/2} - x_{i-1/2}} \int_{x_{i-1/2}}^{x_{i+1/2}} U(x,t^n)\mathrm{d}x,$$

and use the L^1 norm to define accuracy

$$||U^{(\Delta x_i, \Delta t)} - A(U(\cdot,t^n))||_1 = \sum_{\forall i} |\int_{x_{i-1/2}}^{x_{i+1/2}} U_i^n - U(x,t^n)\mathrm{d}x|.$$

Generally, for a first-order scheme the accuracy around a discontinuity turns out to be $\mathrm{O}(\sqrt{(}\Delta x_i))$. To half the error, this means that the grid must be refined and the number of cells is quadrupled. A second-order scheme is often second-order accurate for smooth parts of the solution, but only first-order accurate at discontinuities. If we want to half the error at discontinuities, the number of cells needs to be doubled. Note that schemes with the same order, does not in general have the same accuracy. This means that schemes of the same order for instance introduces different degree of numerical diffusion around a discontinuity.

The global error in the approximation, following [67], is defined by the distance from $U^{(\Delta x_i, \Delta t)}(x,t)$ to the set of all weak solutions $\mathcal{W}$ (in the case that the weak solution U is not unique),

$$\mathcal{W} = \{U : U(x,t) \text{ is a weak solution to the conservation law}\}.$$

To measure the global error, for example the 1-norm over some finite time interval $[0,T]$, denoted by

$$||u||_{1,T} = \int_0^T ||u(\cdot,t||_1 \mathrm{d}t = \int_0^T \int_{-\infty}^{\infty} |u(x,t)|\mathrm{d}x\mathrm{d}t$$

is used. Thus, the global error is defined by

$$\mathrm{dist}(U^{(\Delta x_i, \Delta t)}(x,t), \mathcal{W}) = \inf_{w \in \mathcal{W}} ||U^{(\Delta x_i, \Delta t)}(x,t) - U(x,t)||_{1,T}. \tag{4.9}$$

If the numerical approximation $U^{(\Delta x_i,\Delta t)}(x,t)$ is generated by a conservative and consistent numerical scheme, and if the scheme is stable in some appropriate sense, then the global error $\text{dist}(U^{(\Delta x_i,\Delta t)}(x,t),\mathcal{W}) \to 0$ as $\Delta t \to 0$. There is no guarantee that this is fulfilled for any fixed weak solution $U(x,t)$. However, if the scheme is known to satisfy an discrete form of an entropy condition, convergence to the particular physically relevant weak solution can be proved.

Many numerical schemes have been verified, and for some schemes proved convergent, on simplified test problems. For general systems of equations with arbitrary initial data, no numerical scheme has been proved to be stable or convergent in general, although some convergence results for some schemes has been obtained for special cases, see e.g., [65].

4.3 Flux approximation

In one dimension, the flux over each cell edge is determined by the numerical flux directly. Now, several approaches to approximate the flux (4.5) are introduced. These flux approximations can also be used in the combination with semi-discrete schemes (4.7). Throughout this section, the reconstruction (4.6) yielding that the numerical flux function is a function of $\tilde{H}_{i+1/2} = H(U_i^n, U_{i+1}^n)$. This is used in combination with the notation $U^L = U_i^n$ and $U^R = U_{i+1}^n$, thus

$$\tilde{H}_{i+1/2} = H(U^L, U^R).$$

4.3.1 General approaches

Lax-Friedrichs

The classical numerical scheme named after Peter Lax and Kurt O. Friedrichs, called the *Lax-Friedrichs scheme*, approximates the flux function at each cell edge by the average of the fluxes evaluated immediately to the left and right of the edge,

$$\tilde{H}(U(x_{i+1/2},t^n) = \frac{1}{2}\left(H(U_i^n) + H(U_{i+1}^n)\right).$$

This approximation is called a *centered* approximation. Using this flux approximation, the numerical scheme from [63] reads

$$U_i^{n+1} = U_i^n - \frac{\Delta t}{2\Delta x_i}\left(H(U_{i+1}^n) - H(U_{i-1}^n)\right). \tag{4.10}$$

However, this scheme is unstable. To obtain a stable scheme, an artificial diffusion term $(\Delta x^2/\delta t)U_{xx}$ is added and discretized by the standard central difference. To have the generalization of the Lax-Friedrichs scheme in conservation form (4.4), the Lax-Friedrichs flux approximation is given by

$$\tilde{H}^{LF}(U^L, U^R) = \frac{\Delta x_i}{2\Delta t}\left(U^L - U^R\right) + \frac{1}{2}\left(H(U^L) + H(U^R)\right), \tag{4.11}$$

where $U^L = U_i^n$ and $U^R = U_{i+1}^n$. Note that it is no longer possible to go back to the semi-discrete form, since the artificial diffusion term blows up when $\Delta t \to 0$.

This scheme is known to be very robust and to always converge. However, the convergence is fastidiously slow. The scheme is monotone provided that the CFL condition is fulfilled. One advantage of this scheme is that is avoids the need to solve local Riemann problems arising from the piecewise-constant initial data. The main disadvantage of this first-order scheme, is that it smears both smooth and discontinuous parts of the solution on a coarse grid. This scheme is seldom used in practice.

Second-order flux approximations

By using the midpoint rule to evaluate (4.5), with the midpoint values obtained by (4.10), a second-order centered scheme called the *Lax-Wendroff* scheme is obtained [64]. This flux approximation is given by

$$\begin{aligned} \tilde{H}^{LW}(U^L, U^R) &= H(U^*), \qquad \text{where} \\ U^* &= \frac{1}{2}\left(U^L + U^R\right) - \frac{\Delta t}{2\Delta x_i}\left(H(U^R) - H(U^L)\right). \end{aligned} \tag{4.12}$$

It turns out that this scheme is second-order in both time and space, and it is conditioned stable for linear flux functions. This scheme is known to preserve smooth parts of the solution accurately, but introduce serious oscillations around discontinuities. Furthermore, for general non-linear problems this problem can compute the wrong solution. This is the case for problems with non-convex flux functions.

There are several other classical second-order schemes for hyperbolic PDEs. Popular schemes are the MacCormack scheme [70], the Nessyahu-Tadmor scheme [73], and the Beam-Warming scheme [95]. The average of the Lax-Wendroff and the Beam-Warming scheme results in the Fromm scheme [30]. Another scheme called the leap-frog scheme uses data from two previous time steps. Neither of the mentioned schemes works well for non-linear problems.

FORCE

By taking the arithmetic average of the Lax-Friedrichs and Lax-Wendroff fluxes, the centered *First-Order Centered* (FORCE) flux approximation is obtained in [87],

$$\begin{aligned} \tilde{H}^{FORCE}(U^L, U^R) &= \frac{1}{4}\left(H(U^L) + 2H(U^*) + H(U^R)\right) - \frac{1}{4}\frac{\Delta x_i}{\Delta t}\left(U^R - U^L\right), \qquad \text{where} \\ U^* &= \frac{1}{2}\left(U^L + U^R\right) - \frac{\Delta t}{2\Delta x_i}\left(H(U^R) - H(U^L)\right). \end{aligned} \tag{4.13}$$

The resulting scheme can suffer from the same shortcomings as the Lax-Friedrichs and the Lax-Wendroff schemes. However, for convex flux functions this scheme can perform well and with significantly less smearing than the Lax-Friedrichs scheme. Convergence for this scheme has been established for the isentropic Euler equations and the shallow water equations [22].

Central-upwind

In [59, 60] a centered flux approximation called *central-upwind* was presented. This scheme uses information about the smallest and largest eigenvalue of the Jacobian matrix of the system. Let

$$a^+ = \max_{U\in[U^L,U^R]} \left(\lambda^M, 0\right), \qquad \text{and} \qquad a^- = \min_{U\in[U^L,U^R]} \left(\lambda^m, 0\right),$$

where λ^M and λ^m represent the largest and smallest eigenvalues of the Jacobian matrix of the system, respectively. The values a^+ and a^- estimate how far the Riemann fan across the cell edge $x_{i+1/2}$ extends in the positive and negative directions. The central-upwind flux approximation is given by

$$\tilde{H}^{CU}(U^L,U^R) = \frac{a^+H(U^L) - a^-H(U^R)}{a^+ - a^-} + \frac{a^+a^-}{a^+ - a^-}\left(U^R - U^L\right). \tag{4.14}$$

The upwind nature respect the directions of waves propagating by measuring the one-sided local speeds. The main advantage of the corresponding scheme is that there are no Riemann solvers and characteristic decompositions involved. This makes the scheme applicable for a wide variety of applications. Furthermore, the scheme introduces less numerical dissipation than the first-order schemes mentioned so far. However, there exists no convergence proof for a general non-linear hyperbolic problem for this scheme. For a monotone flux function in the scalar case, this scheme reduces to the classical upwind scheme.

Godunov

In [37] the *Godunov* flux approximation was introduced. If $U(x,t^n) = U_i^n$ in each grid cell Ω_i, the evolution of U can be decomposed into a set of local Riemann problems

$$\begin{aligned} U_t + H(U)_x &= 0, \\ U(x,0) &= \begin{cases} U^L, & x < x_{i+1/2}, \\ U^R, & x \geq x_{i+1/2}. \end{cases} \end{aligned}$$

The Godunov flux approximation is then based on solving these local Riemann problems on each cell edge. For a scalar conservation law this is given by

$$\tilde{H}^G(U^L,U^R) = \begin{cases} \min\limits_{U\in[U^L,U^R]} H(U), & \text{when} \quad U^L \leq U^R, \\ \max\limits_{U\in[U^R,U^L]} H(U), & \text{when} \quad U^L > U^R. \end{cases} \tag{4.15a}$$

In the context of having a flux function with a spatial discontinuity the following modified Godunov flux approximation, which also is valid for a continuous flux, was presented in [1]. If the flux function $H(U)$ has one global maximum $(\theta, H(\theta))$ and no local minimum for the range of U, the Godunov flux approximation reads

$$\tilde{H}^G(U^L,U^R) = \min\left[H\left(\min\left(U^L,\theta\right)\right), H\left(\max\left(\theta,U^R\right)\right)\right]. \tag{4.15b}$$

If the flux function $H(U)$ has one global minimum $(\theta, H(\theta))$, and no local maximum, the Godunov flux approximation reads

$$\tilde{H}^G(U^L, U^R) = \max\left[H\left(\max\left(U^L, \theta\right)\right), H\left(\min\left(\theta, U^R\right)\right)\right]. \tag{4.15c}$$

To ensure that the solution of the Riemann problem on each cell edge not is influenced by the waves from the neighboring cell edge, the time step Δt must be limited by the CFL condition. For scalar problems the corresponding Godunov scheme is monotone if the CFL condition is fulfilled. This scheme is the least diffusive scheme of the schemes presented so far, at least for general scalar problems. The disadvantage of the Godunov scheme is that the scheme requires the solution of Riemann problems. In general, this is computationally expensive and it is well known that solving these local Riemann problems for a system of conservation laws is challenging. For a class of 2×2 systems of conservation laws there exists some stability and convergence theory in, e.g., [65]. More recent results can be found in, e.g., [16], where it is shown convergence and L^1-stability for this scheme when applied to systems with data that have small total variation using probability theory.

For the special application of polymer flooding, the corresponding Riemann problem was solved in Section 3.4.2 and the corresponding Godunov flux approximation can be defined in a straightforward manner, see e.g., [4]. In our experience, not unexpectedly, the first-order Godunov scheme has the least numerical dissipation, also for the polymer system. Furthermore, for monotone, convex, and concave flux functions for this system, the scheme is applicable but computationally expensive. Note however, that the restrictions on the adsorption term $a(c)$ mentioned in Section 3.4.2 are necessary to solve the Riemann problems involved.

4.3.2 The upstream mobility flux

For two-phase flow in porous media, a numerical flux approximation called *upstream mobility flux* has been developed, and can be found in, e.g., [11, 15]. This is an ad-hoc flux approximation which corresponds to an approximate solution to the Riemann problem. To present this flux approximation, the one-dimensional mass-conservation equation for the wetting phase of two-phase flow (2.14) is considered.

The upstream mobility flux approximation is based on simple physical considerations and calculating the mobility λ_α in the correct upstream direction. The direction of the flow is from regions of higher to lower pressure. Thus, the direction of the flow over each cell edge $x_{i+1/2}$ can be found by evaluating

$$\operatorname{sign}\left(p_{w,i+1} - p_{w,i} - g\rho_w \Delta x_i\right).$$

In [81] this is rewritten in terms of the total Darcy velocity v and an implicit formula of the mobility over the cell edge $x = x_{i+1/2}$ is given by

$$\lambda^n_{\alpha,i+1/2} = \begin{cases} \lambda_\alpha(s^n_i), & \text{if} \quad v + \lambda_{\beta,i+1/2}\left(g_\alpha - g_\beta\right) \geq 0, \\ \lambda_\alpha(s^n_{i+1}), & \text{if} \quad v + \lambda_{\beta,i+1/2}\left(g_\alpha - g_\beta\right) < 0, \end{cases}$$

where $\alpha \neq \beta$ and s_i^n denotes the numerical approximation of the saturation of the wetting phase in cell i. In practice, an implicit calculation of mobilities is usually part of an iterative process. In [15] an explicit formula is given, let

$$\begin{aligned} \theta_1 &= v + \lambda_n(s_i^n)(g_w - g_n), \qquad \text{and} \\ \theta_2 &= v + \lambda_w(s_{i+1}^n)(g_n - g_w), \end{aligned}$$

then the mobilities over the cell edge $x = x_{i+1/2}$ are given by

$$\lambda_{w,i+1/2}^n = \begin{cases} \lambda_w(s_i^n), & \text{if} \quad 0 \leq \theta_1 \leq \theta_2, \\ \lambda_w(s_{i+1}^n), & \text{if} \quad \theta_1 \leq 0 \leq \theta_2, \end{cases} \tag{4.16a}$$

$$\lambda_{n,i+1/2}^n = \lambda_n(s_i^n). \tag{4.16b}$$

For the special case where the hyperbolic conservation law (3.3) represents two-phase flow, $s = U$ and $f(s) = H(U)$. Then, the upstream mobility flux approximation can be used and is given by

$$\tilde{H}^{UM}(U^L, U^R) = \frac{\lambda_{w,i+1/2}^n}{\lambda_{w,i+1/2}^n + \lambda_{n,i+1/2}^n} \left(v + \lambda_{n,i+1/2}^n (g_w - g_n) \right), \tag{4.17}$$

where $\lambda_{w,i+1/2}^n$ and $\lambda_{n,i+1/2}^n$ are given by (4.16a-4.16b).

This flux approximation is used in most commercial reservoir simulators. For two-phase flow in a homogeneous media the corresponding scheme is unconditionally monotone, and proved to be convergent in [15, 81]. However, for two-phase counter-current flow in a heterogeneous media no convergence proof exists and the performance of the scheme is discussed in papers A and B.

Remark

Although not mentioned explicitly in the presentation of the different schemes above, numerical schemes are divided into two categories: upwind and non-upwind or centered schemes. The main distinction is that upwind schemes somehow exploits the solution of the Riemann problem, whilst the centered schemes do not. Typically, if the solution of the corresponding Riemann problem is not available, or to computationally expensive to compute, the only option is to adapt centered approaches. Within this family of schemes, it is shown that the Lax-Friedrichs scheme is the least accurate one [22].

4.4 High-resolution schemes

First-order schemes can introduce too large amounts of numerical dissipation so that shocks or discontinuities are smeared and poorly resolved on the grid. Classical second-order methods such as Lax-Wendroff have been shown to give oscillatory approximations to discontinuous solutions. Schemes that are at least second-order accurate

on smooth parts of the solutions, and yet give well-resolved, non-oscillatory discontinuities are called *high-resolution schemes*. These schemes use non-linear dissipation mechanisms to provide solutions without spurious oscillations. From the numerical solution at one time-step, a higher-order representation of the data can be computed, often in the form of polynomials. This representation serves as initial data for the next time step.

The terms high-order and high-resolution are often used interchangeably and loosely in the literature. High-order often refers to any method of order two or higher, including those that are oscillatory. Sometimes the term "very high-order" is used for methods of at least third order. A high-resolution scheme can have a lower order of accuracy, but yield much smaller errors on a given mesh, on which a high-order scheme might give larger errors.

Two versions of high-resolution schemes are *flux-limiter schemes* and *slope-limiter schemes* [68]. In the flux-limiter schemes, let $\tilde{H}^{low}_{i+1/2}$ be a low-order flux (i.e., Lax-Friedrichs (4.11)) and let $\tilde{H}^{high}_{i+1/2}$ be a high-order flux (i.e., the Lax-Wendroff flux (4.12)). Then, using the flux

$$\tilde{H}^n_{i+1/2} = \tilde{H}^{low}_{i+1/2} + \theta^n_i \left(\tilde{H}^{high}_{i+1/2} - \tilde{H}^{low}_{i+1/2} \right)$$

in (4.4) gives a high-resolution scheme for an appropriate *limiter function* $\theta^n_i(U^n_i)$ that is close to unity if U is smooth, and close to zero if U is discontinuous. This approach will not be further discussed here, and the rest of the section is devoted to presenting the approach of slope-limiter schemes.

4.4.1 REA

The general *Reconstruct Evolve Average* (REA) algorithm was originally proposed in [37] as a method for solving the non-linear Euler equations of gas dynamics. It consists of the following steps:

(1) Reconstruct a function $\tilde{U}(x,t^n)$, defined for all x, from the known cell averages U^n_i to obtain one-sided point-values.

(2) Evolve the differential equation, exactly or approximately, with $\tilde{U}(x,t^n)$ as initial data, to obtain $\tilde{U}(x,t^{n+1})$ time Δt later.

(3) Average the evolved solution $\tilde{U}(x,t^{n+1})$ over each cell to obtain new cell averages U^{n+1}_i.

A constant reconstruction like (4.6) results in a first-order scheme, linear reconstruction gives second-order, quadratic gives third-order, and so on. Different linear reconstructions will be presented shortly.

4.4.2 TVD reconstructions

To obtain accuracy better than first-order, the piecewise constant reconstruction (4.6) must be improved. The question is how to interpolate from cell averages to point-values. The interpolant must be conservative, non-oscillatory and sufficiently accurate.

Now, the notation $U^R_{i-1/2}$ and $U^L_{i+1/2}$ is introduced. The value $U^R_{i-1/2}$ is the reconstructed value at the cell edge $x_{i-1/2}$ constructed from the cell to the right (R) of the edge $x_{i-1/2}$, that is cell i. Likewise, the value $U^L_{i+1/2}$ is the reconstructed value at the cell edge $x_{i+1/2}$ constructed from the cell to the left (L) of the edge $x_{i+1/2}$, that is cell i. Thus, at each cell edge there are two reconstructed values originating from both of the adjacent cells. This is illustrated in Figure 4.2.

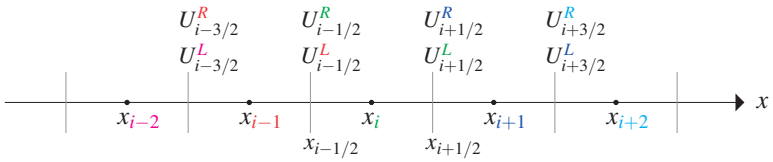

Figure 4.2: At each cell edge there are two reconstructed values $U^L_{i\pm j/2}$ and $U^R_{i\pm j/2}$, originating from a function that contains the slope in the adjacent cells.

Now, a piecewise linear reconstruction is introduced:

$$U^R_{i-1/2} = U^n_i - \frac{1}{2}\delta^n_i,$$
$$U^L_{i+1/2} = U^n_i + \frac{1}{2}\delta^n_i,$$

where δ^n_i is the slope on the i-th cell. The linear function in the i-th cell is designed in such a way that the cell average of the i-th cell is exactly U^n_i. To obtain a second-order accurate method, a nonzero slope δ^n_i is chosen in such a way that U^n_i approximates U_x over the i-th grid cell. Some candidates for the nonzero slope are

$$\delta^n_i = \begin{cases} U^n_i - U^n_{i-1}, & \text{upwind slope,} \\ U^n_{i+1} - U^n_{i-1}, & \text{downwind slope,} \\ \frac{1}{2}\left(U^n_{i+1} - U^n_{i-1}\right), & \text{centered slope.} \end{cases}$$

Note that the cell average resulting from these slopes is unchanged, thus the reconstructions are conservative. The piecewise linear reconstructions resulting from these three choices of the slope δ^n_i are illustrated in Figure 4.3. The upwind, downwind, and centered slopes are all based on the assumption that the solution is smooth. Thus, applying this slope near a discontinuity could introduce oscillations in the slope and consequently in the reconstructed solution. The choice of slope therefore depends on how the solution is behaving near the i-th cell, using a given slope δ^n_i.

Near a discontinuity it can be favorable to limit the slope using a value that is smaller in magnitude in order to avoid oscillations. Methods based on this approach are called *slope-limiter methods*. This concept was first introduced in a series of papers [92–94].

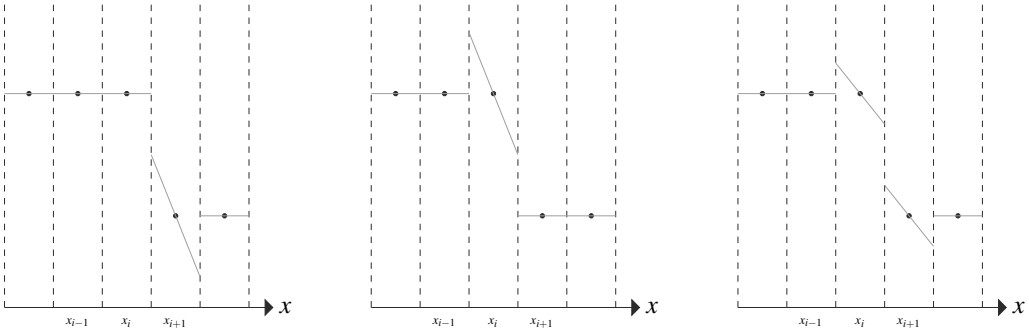

(a) Upwind slope. (b) Downwind slope. (c) Centered slope.

Figure 4.3: Reconstructed function $\tilde{U}(x,t^n)$ with different candidates for the slope δ_i^n in solid lines together with the values for the cell averages U_i^n dotted.

A slope that gives second-order accuracy for smooth solutions is the *minmod slope*

$$\delta_i^n = \text{minmod}\left(U_i^n - U_{i-1}^n, U_{i+1} - U_i\right),$$

where

$$\text{minmod}(a,b) = \begin{cases} a, & \text{if} \quad |a| < |b| \quad \text{and} \quad ab > 0, \\ b, & \text{if} \quad |b| < |a| \quad \text{and} \quad ab > 0, \\ 0, & \text{if} \quad ab \leq 0. \end{cases}$$

This limiter compares the upwind and downwind slopes and chooses the one that is smaller in magnitude. If the slopes have different signs, the slope is set to zero.

Other limiters that do not reduce the slope as much as the minmod near the discontinuity can achieve sharper resolution of discontinuities. For example, the *superbee limiter* introduced in [79] compares each one-sided slope to two times the other one-sided slope. This slope limiter is given by

$$\delta_i^n = \text{maxmod}\left(\delta_i^{1,n}, \delta_i^{2,n}\right),$$

where

$$\delta_i^{1,n} = \text{minmod}\left(U_{i+1}^n - U_i^n, 2\left(U_i^n - U_{i-1}^n\right)\right),$$
$$\delta_i^{2,n} = \text{minmod}\left(2\left(U_{i+1}^n - U_i^n\right), U_i^n - U_{i-1}^n\right),$$

and

$$\text{maxmod}(a,b) = \begin{cases} a, & \text{if} \quad |a| > |b| \quad \text{and} \quad ab > 0, \\ b, & \text{if} \quad |b| > |a| \quad \text{and} \quad ab > 0, \\ 0, & \text{if} \quad ab \leq 0. \end{cases}$$

The superbee limiter results in a steeper reconstruction than the minmod limiter, thus adding less numerical viscosity to the scheme.

Different modifications of the minmod and superbee limiter are also used in the literature. One popular limiter is the *monotonized central-difference limiter* introduced with $\theta = 2$ in [93]:

$$\delta_i^n = \text{minmod}\left(\theta\left(U_i^n - U_{i-1}^n\right), \frac{1}{2}\left(U_{i+1}^n - U_{i-1}^n\right), \theta\left(U_{i+1}^n - U_i^n\right)\right), \qquad \theta \in [1,2].$$

In Figure 4.4 the minmod and superbee limiters are applied to a discontinuity smeared over two cells.

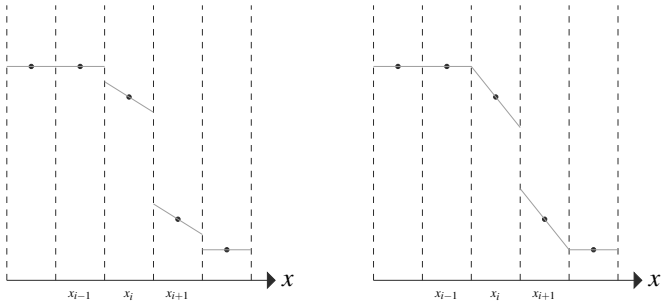

(a) Minmod slope.

(b) Superbee limiter.

Figure 4.4: Reconstructed function $\tilde{U}(x,t^n)$ with different candidates for the slope δ_i^n in solid lines together with the values for the cell averages U_i^n dotted.

At a discontinuity we cannot expect to maintain high-order accuracy. However, when limiting the slope, the nonlinearity introduced in the scheme ensures that the solution is non-oscillatory and TVD for scalar equations.

For systems of conservation laws, the solution is not necessarily TVD, but it is customary to apply the same reconstruction as for scalar equations.

4.4.3 ODE solver

The semi-discrete approach introduced in Section 4.1.2 is particularly useful when dealing with higher-order methods. This framework allows for decoupling of spatial and temporal accuracy. Note that the rest of this section focuses on higher-order accuracy in space. To retain high-order accuracy in time without creating spurious oscillations, one can use a TVD Runge-Kutta method as the ODE solver [38, 83]. These schemes are designed to maintain the TVD property (4.8) and employ a combination of forward Euler steps to advance the solution in time. Let R_i denote

$$R_i(U(t)) = -\frac{1}{\Delta x}\left(\tilde{H}_{i+1/2}(t) - \tilde{H}_{i-1/2}(t)\right).$$

In [83] the general Runge-Kutta scheme for (4.7) is written in the form

$$\begin{aligned} U^{(0)} &= U^n, \\ U^{(j)} &= \sum_{k=0}^{j-1} \left(\alpha_{jk} U^{(k)} + \Delta t \beta_{jk} R(U^{(k)}) \right), \qquad j = 1, \cdots, m, \\ U^{(m)} &= U^{n+1}. \end{aligned} \tag{4.18}$$

The optimal choices of the coefficients α_{jk} and β_{jk} for the general Runge-Kutta scheme (4.18) to be TVD are found in [83]. The second-order TVD Runge-Kutta method reads:

$$\begin{aligned} U_i^{(1)} &= U_i^n + \Delta t R_i(U^n), \\ U_i^{n+1} &= \frac{1}{2} U_i^n + \frac{1}{2} \left[U_i^{(1)} + \Delta t R_i(U^{(1)}) \right]. \end{aligned} \tag{4.19}$$

Similarly, the third-order TVD Runke-Kutta methods read:

$$\begin{aligned} U_i^{(1)} &= U_i^n + \Delta t R_i(U^n), \\ U_i^{(2)} &= \frac{3}{4} U_i^n + \frac{1}{4} \left[U_i^{(1)} + \Delta t R_i(U^{(1)}) \right], \\ U_i^{n+1} &= \frac{1}{3} U_i^n + \frac{2}{3} \left[U_i^{(2)} + \Delta t R_i(U^{(2)}) \right]. \end{aligned} \tag{4.20}$$

In [38] a simple but illustrating numerical example shows that it is in general much safer to use a TVD Runge-Kutta method to avoid oscillations in hyperbolic problems.

4.5 Applications

In this section, the numerical framework presented throughout this chapter is related to the applications presented in Section 2.2. For the application of homogeneous two-phase flow, the framework is straightforward. However, for the application of heterogeneous two-phase flow, extra care must be taken around the discontinuity interface $x = x_h$. The framework presented is for a general system of hyperbolic conservation laws, and the application of polymer flooding needs to be put into this framework. Finally, the numerical framework of the model equations of CO_2-injection needs to be discussed.

4.5.1 Heterogeneous two-phase flow

In Section 3.3 a spatial discontinuity was introduced across the interface $x = x_h$ in the flux function $h(u)$ of the scalar one-dimensional hyperbolic conservation law (3.4a). The flux function corresponding to the application of heterogeneous two-phase flow was set into this framework in Section 3.3.4. Now, some comments regarding the numerical flux approximation (4.5) of the heterogeneous version of the model (2.14) are given.

The governing equation and the flux function is given by

$$\begin{aligned} &\phi s_t + f(s)_x = 0, \\ &\text{with} \qquad f(s) = \begin{cases} f^L(s) = \frac{\lambda_w^L}{\lambda_w^L+\lambda_n^L}\left(v+\lambda_n^L(g_w-g_n)\right), & x < x_h, \\ f^R(s) = \frac{\lambda_w^R}{\lambda_w^R+\lambda_n^R}\left(v+\lambda_n^R(g_w-g_n)\right), & x \geq x_h. \end{cases} \end{aligned} \tag{4.21}$$

Let $\phi = 1$ and let the spatial discontinuity at $x = x_h$ be located at cell edge $x_{d+1/2}$. The corresponding finite-volume scheme in conservation form (4.4) reads

$$s_i^{n+1} = \begin{cases} s_i^n - \frac{\Delta t}{\Delta x}\left(\tilde{F}^L_{i+1/2} - \tilde{F}^L_{i-1/2}\right), & \text{if} \quad x_i \leq x_{d-1}, \\ s_i^n - \frac{\Delta t}{\Delta x}\left(\tilde{F}^D_{i+1/2} - \tilde{F}^D_{i-1/2}\right), & \text{if} \quad x_{d-1} < x_i < x_{d+2}, \\ s_i^n - \frac{\Delta t}{\Delta x}\left(\tilde{F}^R_{i+1/2} - \tilde{F}^R_{i-1/2}\right), & \text{if} \quad x_i \geq x_{d+2}, \end{cases} \tag{4.22}$$

where the numerical flux $\tilde{F}^L_{i\pm1/2}$ is directly associated with the flux $f^L(s)$ and $\tilde{F}^R_{i\pm1/2}$ is directly associated with the flux $f^R(s)$. Note that $\tilde{F}^D_{i\pm1/2}$ is associated with the flux around the discontinuity $x = x_h$, and extra care must be taken. If the flux functions $f^L(s)$ and $f^R(s)$ have one global maximum, and no local minima for $s \in (0,1)$, and $f^L(0) = f^R(0)$ and $f^L(1) = f^R(1)$, then (4.15b) implies

$$\tilde{F}^D(s^L, s^R) = \min\left[f^L\left(\min\left(s^L, \theta_{f^L}\right)\right), f^R\left(\max\left(\theta_{f^R}, s^R\right)\right), f^L(A)\right],$$

for the Godunov flux approximation, where $(\theta_{f^L}, f^L(\theta_{f^L}))$ and $(\theta_{f^R}, f^R(\theta_{f^R}))$ represent the maximum points of f^L and f^R, respectively. The value A comes from the choice of $\{A,B\}$-connection discussed in Section 3.3.2.

4.5.2 Polymer flooding

The general conservative finite-volume scheme (4.4) for the system of equations governing polymer flooding (3.21) is written as

$$\begin{aligned} s_i^{n+1} &= s_i^n - \frac{\Delta t}{\Delta x}\left(F_{i+1/2} - F_{i-1/2}\right), \\ s_i^{n+1}c_i^{n+1} + a(c_i^{n+1}) &= s_i^n c_i^n + a(c_i^n) - \frac{\Delta t}{\Delta x}\left(G_{i+1/2} - G_{i-1/2}\right), \end{aligned} \tag{4.23}$$

where the numerical fluxes $F_{i\pm1/2}$ and $G_{i\pm1/2}$ are associated with the flux functions $f(s,c)$ and $g(s,c) = cf(s,c)$. As discussed throughout the previous sections, the choice of numerical flux approximation and reconstruction determines the numerical scheme. To recover the polymer concentration c_i^{n+1} from the second equation of (4.23), the saturation s_i^{n+1} from the first equation of (4.23) is used in an iterative method like Newton-Rhapson.

The modified Godunov flux approximation that was presented for a spatial conservation law with discontinuous flux function in [1], was in [4] extended to the polymer system.

The polymer concentration $c(x,t)$ in $f(s,c)$ is treats as known function which may be discontinuous at the space discretization points. For this reason, on the edge of each cell i the following conservation law is considered:

$$s_t + f(s,c_i^n)_x = 0,$$

with initial condition $s(x,t^n) = s_i^n$ for $x \in (x_{i-1/2}, x_{i+1/2})$. Thus, using the modified Godunov flux approximation (4.15b) for a flux function attaining one global maximum and no local minima the DFLU flux is defined as

$$\tilde{F}_{i+1/2}^{DFLU}(s_i^n, c_i^n, s_{i+1}^n, c_{i+1}^n) = \min\left[f(\min(s_i^n, \theta_i^n), c_i^n), f(\max(s_{i+1}^n, \theta_{i+1}^n), c_{i+1}^n)\right],$$

where $\theta_i^n = \text{argmax} f(\cdot, c_i^n)$.

In [4] a discussion on total variation bounds and a convergence analysis for the DFLU scheme applied to the polymer system is provided. Note that the saturation s do not need to be of total variation bounded since $f(s,c)$ and $c(x,t)$ is discontinuous. Furthermore, in [4] it is concluded that the convergence of (s_i^n, c_i^n) is difficult to prove for general flux functions unless the polymer concentration c is Lipschitz continuous.

4.5.3 CO_2 migration

So far, the numerical framework presented herein is only subject to hyperbolic conservation laws. The modeling framework for the application of CO_2 migration in a saline aquifer presented in Section 2.2.3 includes both an elliptic pressure equation, and a hyperbolic saturation equations. Thus, some remark about the numerical solution strategy in Paper D following [33] must be made. The elliptic pressure equation is formulated from the mass conservation equations (2.23) and (2.26). For an incompressible system, conservation of volume can be considered instead of mass. From Section 2.2.3 we remember that the total volume has contribution from the volume of pure brine, the volume of the CO_2 mixture, and the volume of the brine mixture. The component masses M^n and M^w can be expressed in terms of these volumes to obtain a pressure equation on the form

$$\nabla \cdot \Big[(\zeta_T - \zeta_M)\, \mathbf{v}_{n,x_3\in(\zeta_M,\zeta_T]} + (\zeta_M - \zeta_R)\, \mathbf{v}_{w,x3\in(\zeta_R,\zeta_M]} + (\zeta_R - \zeta_D)\, \mathbf{v}_{w,x_3\in(\zeta_D,\zeta_R]} + (\zeta_D - \zeta_B)\, \mathbf{v}_{w,x_3\in[\zeta_B,\zeta_D]} \Big] = V_\phi C_R,$$

where V_ϕ is the volume change due to dissolution per unit mass of CO_2 dissolved. The pressure is obtained using a standard implicit solver for the pressure equation, with a harmonic average for the permeability. Next, the masses M^w, M^n are updated through an explicit solver for the hyperbolic equations (2.23) and (2.26), using upstream-weighted mobility values in the flux approximation. The location of the interface ζ_M is found similarly through the discretization of (2.27), and the interfaces ζ_R and ζ_D are calculated from the updated masses and ζ_M while honoring the constraint

$$\zeta_B \le \zeta_D \le \zeta_R \le \zeta_M \le \zeta_T.$$

This framework is called an IMplicit Pressure Explicit Saturation (IMPES) framework. However, the main focus in Paper D was not on the numerical framework, and for this reason the framework was only briefly outlined in this presentation.

4.6 Other approaches

The literature and research on efficient, yet accurate, solvers for hyperbolic conservation laws is extensive and there are several numerical approaches which have not been mentioned here. Classical textbooks on this framework are [36, 57, 66, 67, 87, 88]. Furthermore, many numerical approaches has been applied in a problem specific manner not necessarily applicable for general problems.

For high-resolution numerical schemes we briefly mention the *essentially non-oscillatory* (ENO) reconstruction approach. This reconstruction procedure was introduced in 1987 by Harten et al. in [40]. The same idea that the slope-limiter methods are based on may be extended to higher-order polynomials by choosing which cells to interpolate over for each cell i, such that the interpolant introduces the least oscillation. Thus, the interpolation in this reconstruction is performed over a variable, data-dependent, stencil. Later, a *weighted* ENO (WENO) scheme was introduced in [50, 69] by using all possible stencils rather than choosing only one. A weighted combination of the stencils is used, where the weights are such that smoother approximations have greater weight.

The *discontinuous Galerkin* approach [24] can also be applied for generating arbitrarily high-order schemes for hyperbolic conservation laws. This consists of rewriting the conservation law in weak form, see, e.g., [25]. Another well-know approach that is known to compute solutions with little numerical diffusion is *front-tracking* combined with dimensional splitting [43]. The approach consists of representing the solution as a set of discontinuities and propagate in time. The speed of the shocks can be computed by Rankine-Hugoniot, whilst the rarefaction wave can be approximated by a sequence of small shocks. These schemes are well-suited to follow fronts in the solution, which can either be tracked on a cartesian grid with some dimensional splitting, or a streamline method can be applied.

For the polymer system and systems that are similar, some selected high-order approaches will now be listed. A TVD implicit flux-limiting scheme for black oil is discussed in [80]. In [14] a higher-order Godunov scheme for general systems of hyperbolic conservation laws is developed and investigated. This scheme is found to reduce smearing of fronts. The use of this second-order Godunov-type scheme was applied to the polymer system in [44] and found to perform well compared to standard finite-difference schemes. In [56] a high-order Godunov scheme was combined with adaptive mesh refinement and applied to a realistic north-sea polymer flood. The accuracy of first- and higher-order schemes in an ENO setting was investigated for an enhanced condensate process in [49, 90]. The front-tracking approach was applied in [41] for the polymer flooding problem, and to a similar miscible gas injection problem in [53]. Another approach for the purpose of reducing numerical dispersion using a stream-line based simulator for polymer flooding is investigated in [7].

Chapter 5

Summary of included papers

In this chapter the papers included in Part II are summarized.

5.1 Papers A and B

Motivated by the earlier works [72, 89] the performance of the upstream mobility scheme applied to counter-current, one-dimensional, heterogeneous two-phase flow is investigated. In [72] it was shown that the scheme can converge to the wrong solution when applied to this kind of flow. However, for the examples shown in [72], advection was neglected and the flow was purely a gravity problem. In [89] the upstream mobility scheme was applied to a similar two-phase flow problem where advection was included for general flow where the wetting phase drains the non-wetting phase. For this kind of flow, the scheme was shown to have even larger deviations through numerical experiments. In papers A and B the upstream mobility scheme is applied to the counter-current flow of CO_2 and brine in a 1D vertical column for the purpose of evaluating the performance of the scheme applied to a practical example.

When we say that the upstream mobility scheme fails, has deviations, or is erroneous, this is compared to the numerical solution computed with what is interpreted to give the physically meaningful solution. Both [72, 89] and the investigations in papers A and B compare the solution produced by the upstream mobility scheme with the solution produced by the Godunov scheme for heterogeneous two-phase flow, using the optimal entropy connection (3.18a)-(3.18b). A complementary discussion on what the *actual* true and physically meaningful solutions is, is given in Section 3.3.4.

For the experiments carried out in these papers, realistic parameters and reservoir settings have been used. The wetting brine phase is denser than the non-wetting CO_2 phase and the CO_2 will flow on top of the brine in a drainage process. The heterogeneity in the rock is introduced through the permeability. In these works we also included experiments where the flux function contained two spatial discontinuities. That is, the rock consisted of three rock types. The relative permeabilities used in papers A and B are based on the classical Brooks-Corey (2.3) and Van-Genuchten relations (2.4), and also cubic interpolation of various datasets. Through numerous numerical experi-

ments we found several situations where the upstream mobility scheme turns out to be ill-conditioned since a small perturbation in the relative permeability may give large difference in the solution computed by the scheme. Furthermore, we saw that the scheme lacks entropy consistency, since regardless of which available entropy solution the upstream mobility scheme is compared with, there are cases in which the scheme will not converge to any of these solutions.

Since realistic reservoirs consists of several rock types, approximating the numerical flux across spatial discontinuities correctly is crucial to capture the correct flow behavior. The findings of this work shows that this is not a trivial task, and the extensive use of the upstream mobility scheme should be reconsidered. We emphasize that this performance was only found for some specific experiments and that the upstream mobility scheme performs well in most cases. Nevertheless, since the upstream mobility scheme is widely used for reservoir simulation, it is important to be aware that the scheme can be ill-conditioned and lack entropy consistency.

5.2 Paper C

In Section 2.2.2 the polymer flood model were derived. This system, or similar systems of equations was studied in [48, 51, 52, 85]. The more complicated model including adsorption we have used in this work, was analyzed by [51]. However, this was only for horizontal flow. For this situation the eigenvalues of the corresponding Jacobian matrix is positive and the construction of Godunov flux approximation is less difficult. In [4] the similar problem is considered including gravity in a down-dip formulation and several first-order flux approximations are used to solve the one-dimensional problem.

Traditionally, high-resolution schemes has been applied to simple models. In Paper C, high-resolution numerical schemes are applied to the polymer flood model where the effect of adsorption of polymer molecules onto the reservoir rock and the resulting water permeability reduction are included. The motivation for applying high-resolution schemes to this system is that unlike water fronts in the classical two-phase flow system, the linear waves describing the polymer bank are not self-sharpening. Resolving these waves is essential to accurately predict the enhanced oil recovery from adding polymer to the water. This can be challenging using standard low-order numerical schemes, since their numerical diffusion will tend to smooth the polymer bank and hence fail to accurately resolve the enhanced oil recovery effect.

The performance of different first- and higher-order schemes are evaluated and discussed for different flow situations through numerical experiments. Different flow situations include up-, down-, and horizontal flow, varying adsorption term, and varying permeability reduction. Through numerous numerical experiments we show that the high-resolution schemes give better accuracy than the first-order schemes, as expected. Furthermore, some special numerical artifacts of the polymer flooding are found and presented in this paper. These artifacts can be divided into the following five sub-cases: (1) comparing two numerical experiments, where the only difference is the inclusion of adsorption, we found that the superbee limiter can introduce oscillations in the satura-

tion front, (2) for a special flow case we found that the superbee limiter underestimates the propagation speed of the saturation front compared to other reconstructions, (3) when the flooding problem develop an oil bank just ahead of a contact discontinuity, it is particularly hard to model on a coarse scale, (4) the introduction of a so-called false oil bank, where the reference solution has a constant saturation profile whilst the coarse scale approximations has a dip in saturation, and (5) the coarse-scale approximation of the polymer front has varying numerical diffusion, depending on which flow case we are considering and how adsorption is modeled.

The occurrence of these numerical artifacts are quantified and summarized in the included paper. We saw that the superbee limiter can introduce oscillations and over- or underestimate the propagation speed of the saturation front in some cases. Even when applying a constant reconstruction the propagation speed for the contact discontinuity of the polymer concentration can be over- or underestimated. The minmod limiter seems to be the safest choice, even though some of the numerical artifacts was found also for this slope limiter. Sub-case (5) means that the propagation speed of the polymer front can be over- or underestimated. Especially in two dimensions, this can have a large effect on the overall flow. The findings of this papers contributes to increased knowledge and understanding of high-resolution schemes for realistic applications like the polymer flooding system.

5.3 Paper D

In Paper D the ongoing CO_2 injection at the Utsira (Sleipner) formation in the North-Sea is considered as a numerical field-scale study for CO_2 storage. In addition to the standard physics of two-phase flow, the upscaled model used in this work includes dissolution, effective mixing, and capillary trapping. There are several mechanisms which contribute to the process of dissolution. Firstly, there is diffusion of CO_2 in the brine phase. Secondly, dissolution of CO_2 into brine induces an increase in brine density. Though small, this density increase creates a gravitationally unstable convection of brine saturated with CO_2 above less dense brine, that can transport CO_2 downwards while driving brine with low CO_2 concentration upwards. This convection is referred to as convective mixing and the mechanism accelerates the rate at which CO_2 is dissolved. The upscaled rate of this mechanism is the main focus of this paper.

To model the CO_2-migration in the topmost layer of the Utsira formation we rely on the gravimetric data reported by Alnes et al. [6] together with the available geometric, petrophysical and measured data. Combining these data with the mentioned upscaled model, we obtain the first field-scale estimates of the effective upscaled convective mixing rates. To account for the uncertainty associated with the provided data, a sensitivity study relative to the most uncertain parameters is performed. The study results in rates that range from 0 to 30 kg/m^2/year, and the most likely scenario, using the upper limit that at most 1.8% of the injected CO_2 dissolves per year from [6], leads to an estimate of upscaled convective mixing on the order of 15 kg/m^2/year, which is on the same order of magnitude as the results from theoretical studies (see, e.g., [29]). In particular, we note that the relatively high estimates of dissolved CO_2 cannot be understood

without the mechanism of convective mixing.

It is concluded that convective mixing may be an important mechanism on the field scale, even during the injection period. Using available data, it is possible to quantify the effective upscaled parameter, which is important for long-term storage efficiency analysis.

5.4 Conclusions and future directions

The classical upstream mobility scheme has been shown to be ill-conditioned and to lack entropy consistency for realistic cases of one-dimensional, counter-current, heterogeneous, two-phase flow. These findings are important due to the extensive use of the upstream mobility scheme in the reservoir simulation community. Furthermore, in the wake of these findings a discussion regarding what can be considered to be the physically relevant entropy condition has occurred in the literature [9].

High-resolution schemes have been applied to the polymer flood system and not unexpectedly found to be more accurate than traditional low-order schemes. Furthermore, the high-resolution numerical schemes were found to give rise to some numerical artifacts. These artifacts are summarized and quantified for what situations they are expected to occur. Especially, the finding that the propagation speed of the polymer front can be over- or underestimated for different flooding situations can influence a two-dimensional system. In realistic applications, the topography can give rise to both down dip and up dip flow resulting in deviations between the approximated propagation speed in the different directions. This needs to be investigated further. Furthermore, more complicated representations of adsorption and permeability reduction can influence the applicability of the schemes. Other properties like the degree of mixing between water and polymer, and inaccessible pore volume can also influence the results. In realistic applications, the solution of the corresponding Riemann problem is not known and more knowledge on high-resolution schemes applied to the polymer system can give valuable insight for this problem.

For CO_2 sequestration it is concluded that convective mixing may be an important mechanism on the field scale, even during the injection period. Using available data from the Utsira formation, we quantified the effective upscaled parameter for convective mixing. For long-term storage analysis this parameter can be applied and contribute to better knowledge of the contribution of solubility trapping to the total trapping of CO_2. Applying this upscaled parameter to other CO_2 sequestration projects, either ongoing or theoretical, further sensitivity analysis to the most uncertain parameters should be done.

Bibliography

[1] ADIMURTHI, JAFFRÉ, J., AND VEERAPPA GOWDA, G. D. Godunov-type methods for conservation laws with a flux function discontinuous in space. *SIAM Journal on Numerical Analysis 42*, 1 (2004), 179–208.

[2] ADIMURTHI, MISHRA, S., AND VEERAPPA GOWDA, G. D. Optimal entropy solutions for conservation laws with discontinuous flux-functions. *Journal of Hyperbolic Differential Equations 2*, 4 (2005), 783–837.

[3] ADIMURTHI, AND VEERAPPA GOWDA, G. D. Conservation law with discontinuous flux. *Journal of Mathematics of Kyoto University 43*, 1 (2003), 27–70.

[4] ADIMURTHI, VEERAPPA GOWDA, G. D., AND JAFFRÉ, J. The DFLU flux for systems of conservation laws. *Journal of Computational and Applied Mathematics 247* (2013), 102–123.

[5] ALLAN FREEZE, R., AND CHERRY, J. A. *Groundwater*. Prentize Hall, 1977.

[6] ALNES, H., EIKEN, O., NOONER, S., SASAGAWA, G., STENVOLD, T., AND ZUMBERGE, M. Results from Sleipner gravity monitoring: updated density and temperature distribution of the CO_2 plume. *Energy Procedia 4* (2011), 5504–5511.

[7] ALSOFI, A. M., AND BLUNT, M. J. Control of numerical dispersion in streamline-based simulations of augmented waterflooding. *SPE Journal 18*, 6 (2013), 1–102.

[8] ANDREIANOV, B., AND CANCÈS, C. Vanishing capillarity solutions of Buckley–Leverett equation with gravity in two-rocks' medium. *Computational Geosciences 17*, 3 (2013), 551–572.

[9] ANDREIANOV, B., AND CANCÈS, C. A phase-by-phase upstream scheme that converges to the vanishing capillarity solution for countercurrent two-phase flow in two-rocks media. *Computational Geosciences 18*, 2 (2014), 211–226.

[10] ANDREIANOV, B., KARLSEN, K. H., AND RISEBRO, N. H. A theory of L^1-dissipative solvers for scalar conservation laws with discontinuous flux. *Archive for Rational Mechanics and Analysis 201*, 1 (2011), 27–86.

[11] AZIZ, K., AND SETTARI, A. *Petroleum reservoir simulation*. Applied Science Publishers London, 1979.

[12] BACHU, S. Sequestration of CO_2 in geological media: criteria and approach for site selection in response to climate change. *Energy Conversion and Management 41*, 9 (2000), 953–970.

[13] BEAR, J. *Dynamics of fluids in porous media*. Dover Publications, 1972.

[14] BELL, J. B., COLELLA, P., AND TRANGENSTEIN, J. A. Higher order Godunov methods for general systems of hyperbolic conservation laws. *Journal of Computational Physics 82*, 2 (1989), 362–397.

[15] BRENIER, Y., AND JAFFRÉ, J. Upstream differencing for multiphase flow in reservoir simulations. *SIAM Journal on Numerical Analysis 28*, 3 (1991), 685–696.

[16] BRESSAN, A., AND JENSSEN, H. K. On the convergence of Godunov scheme for nonlinear hyperbolic systems. *Chinese Annals of Mathematics 21*, 3 (2000).

[17] BROOKS, R. H., AND COREY, A. T. Hydraulic properties of porous media. *Hydrology papers, Colorado State University 3* (1964).

[18] BUCKLEY, S. E., AND LEVERETT, M. C. Mechanism of fluid displacements in sands. *Transactions of the AIME 146* (1942), 107–116.

[19] BÜRGER, R., AND KARLSEN, K. H. On a diffusively corrected kinematic-wave traffic model with changing road surface conditions. *Mathematical Models and Methods in Applied Sciences 13*, 12 (2003), 1767–1799.

[20] BÜRGER, R., KARLSEN, K. H., AND TOWERS, J. D. An Engquist-Osher-type scheme for conservation laws with discontinous flux adapted to flux connections. *SIAM Journal on Numerical Analysis 47*, 3 (2009), 1684–1712.

[21] CELIA, M. A., AND NORDBOTTEN, J. M. Practical modeling approaches for geological storage of carbon dioxide. *Groundwater 47*, 5 (2009), 627–38.

[22] CHEN, G.-Q., AND TORO, E. F. Centered difference schemes for nonlinear hyperbolic equations. *Journal of Hyperbolic Differential Equations 1*, 3 (2004).

[23] COATS, K. H., DEMPSEY, J. R., AND HENDERSON, J. H. The use of vertical equilibrium in two-dimensional simulation of three-dimensional reservoir performance. *SPE Journal 11*, 01 (1971), 63–71.

[24] COCKBURN, B., KARNIADAKIS, G. E., AND SHU, C.-W. *The devolpment of discontinous Galerkin methods*. Springer, 2000.

[25] COCKBURN, B., AND SHU, C.-W. TVB Runge-Kutta local projection discontinuous Galerkin finite element method for conservation laws II : General framework. *Mathematics of Computation 52*, 186 (1989), 411–435.

[26] COURANT, R., FRIEDRICHS, K. O., AND LEWY, H. Uber die partiellen Differenzengleiehungen der mathematischen Physik. *Mathematische Annalen 100*, 1 (1928), 32–74.

[27] DANG, C. T. Q., CHEN, Z. J., NGUYEN, N. T. B., BAE, W., AND PHUNG, T. H. Development of isotherm polymer/surfactant adsorption models in chemical flooding. *In Proceedings of SPE Asia Pacific Oil and Gas Conference and Exhibition, 20-22 September, Jakarta, Indonesia* (2011), Society of Petroleum Engineers.

[28] DULLIEN, F. A. L. *Porous Media Fluid Transport and Pore Structure*. Academic Press, 1979.

[29] ELENIUS, M. T., NORDBOTTEN, J. M., AND KALISCH, H. Effects of a capilary transition zone on the stability of a diffusiveboundary layer. *IMA Journal of Applied Mathematics* (2014), accepted.

[30] FROMM, J. E. A method for reducing dispersion in convective difference schemes. *Journal of Computational Physics 3*, 2 (1968), 176–189.

[31] GAO, C. H. Scientific research and field applications of polymer flooding in heavy oil recovery. *Journal of Petroleum Exploration and Production Technology 1*, 2-4 (2011), 65–70.

[32] GASDA, S. E., NORDBOTTEN, J. M., AND CELIA, M. A. Vertical equilibrium with sub-scale analytical methods for geological CO_2 sequestration. *Computational Geosciences 13*, 4 (2009), 469–481.

[33] GASDA, S. E., NORDBOTTEN, J. M., AND CELIA, M. A. Vertically averaged approaches for CO_2 migration with solubility trapping. *Water Resources Research 47*, 5 (2011), W05528.

[34] GIMSE, T., AND RISEBRO, N. H. Riemann problems with a discontinous flux function. *In Proceedings of Third International Conference on Hyperbolic Problems Studentlitteratur, Uppsala, Sweden, June 11-15* (1991), 488–502.

[35] GIMSE, T., AND RISEBRO, N. H. Solution of the Cauchy problem for a conservation law with a discontinous flux function. *SIAM Journal on Mathematical Analysis 23*, 3 (1992), 635–648.

[36] GODLEWSKI, E., AND RAVIART, P.-A. *Numerical approximation of hyperbolic systems of conservation laws*. Springer, 1996.

[37] GODUNOV, S. K. A difference method for numerical calculation of discontinuous solutions of the equations of hydrodynamics. *Matematicheskii Sbornik 89*, 3 (1959), 271–306.

[38] GOTTLIEB, S., AND SHU, C.-W. Total variation diminishing Runge-Kutta schemes. *Mathematics of Computation of the American Mathematical Society 67*, 221 (1998), 73–85.

[39] HARTEN, A. High resolution schemes for hyperbolic conservation laws. *Journal of Computational Physics 49*, 3 (1983), 357–393.

[40] HARTEN, A., AND OSHER, S. J. Some results on uniformly high-order accurate essentially nonoscillatory schemes. *Applied Numerical Mathematics 2*, 3 (1986), 347–377.

[41] HAUGSE, V., KARLSEN, K. H., LIE, K.-A., AND NATVIG, J. R. Numerical solution of the polymer system by front tracking. *Transport in Porous Media 44*, 1 (2001), 63–83.

[42] HESSE, M. A., ORR, F. M., AND TCHELEPI, H. A. Gravity currents with residual trapping. *Energy Procedia 1*, 1 (2009), 3275–3281.

[43] HOLDEN, H., AND RISEBRO, N. H. *Front tracking for hyperbolic conservation laws*. Springer, 2002.

[44] HOLING, K., ALVESTAD, J., AND TRANGENSTEIN, J. A. The use of second-order Godunov-type methods for simulating EOR processes in realistic reservoir models. *In Proceedings of 2nd European Conference on the Mathematics of Oil Recovery, Arles, France, September 11-14* (1990), 101–111.

[45] HUPPERT, H. E., AND WOODS, A. W. Gravity-driven flows in porous layers. *Journal of Fluid Mechanics 292* (1995), 55–69.

[46] INTERGOVERNMENTAL PANEL ON CLIMATE CHANGE (IPCC). Special report on carbon dioxide capture and storage. Tech. rep., Cambridge University Press, 2005.

[47] ISAACSON, E. L. Global solution of a riemann problem for non-strictly hyperbolic system of conservation laws arising in enhanced oil recovery. *In Rockefeller University preprints* (1989).

[48] ISAACSON, E. L., AND TEMPLE, B. The structure of asymptotic states in a singular system of conservation. *Advances in Applied Mathematics 11*, 2 (1990), 205–219.

[49] JESSEN, K., GERRITSEN, M. G., AND MALLISON, B. T. High-resolution prediction of enhanced condensate recovery processes. *SPE Journal* (2008), 257–266.

[50] JIANG, G. S., AND SHU, C.-W. Efficient implementation of weighted ENO schemes. *Journal of Computational Physics 228*, 126 (1996), 202–228.

[51] JOHANSEN, T., AND WINTHER, R. The solution of the Riemann problem for a hyperbolic system of conservation laws modeling polymer flooding. *SIAM Journal on Mathematical Analysis 19*, 3 (1988), 541–566.

[52] JOHANSEN, T., AND WINTHER, R. The Riemann problem for multicomponent polymer flooding. *SIAM Journal on Mathematical Analysis 20*, 4 (1989), 908–929.

[53] JUANES, R., AND LIE, K.-A. A front-tracking method for efficient simulation of miscible gas injection processes. *In Proceedings of SPE Reservoir Simulation Symposium, Houston, Texas, USA, January 31 - February 2* (2005).

[54] JUANES, R., SPITERI, E. J., ORR, F. M., AND BLUNT, M. J. Impact of relative permeability hysteresis on geological CO_2 storage. *Water Resources Research 42*, 12 (2006), W12418.

[55] KAASSCHIETER, E. F. Solving the Buckley–Leverett equation with gravity in a heterogeneous porous medium. *Computational Geosciences 3*, 1 (1999), 23–48.

[56] KHAN, S., AND TRANGENSTEIN, J. A. Application of adaptive mesh-refinement with a new high-order method in simulation of north sea micellar/polymer flood. *In In proceedings of SPE Reservoir Simulation Symposium, 12-15 February, San Antonio, Texas. USA* (1995).

[57] KRÖNER, D. *Numerical schemes for conservation laws*. Wiley Chichester, 1997.

[58] KRUŽKOV, S. N. First order quasilinear equations in several independent variables. *Sbornik: Mathematics 10*, 2 (1970), 217–243.

[59] KURGANOV, A., NOELLE, S., AND PETROVA, G. Semidiscrete central-upwind schemes for hyperbolic conservation laws and Hamilton-Jacobi equations. *SIAM Journal on Scientific Computing 23*, 3 (2001), 707–740.

[60] KURGANOV, A., AND TADMOR, E. New high-resolution central schemes for nonlinear conservation laws and convection–diffusion equations. *Journal of Computational Physics 160*, 1 (2000), 241–282.

[61] LAKE, L. W. *Enhanced oil recovery*. Prentice Hall, 1989.

[62] LANGTANGEN, H. P., TVEITO, A., AND WINTHER, R. Instability of Buckley-Leverett flow in a heterogeneous medium. *Transport in Porous Media 9*, 3 (1992), 165–185.

[63] LAX, P. D. Weak solutions of nonlinear hyperbolic equations and their numerical computation. *Communications on Pure and Applied Mathematics 7*, 1 (1954), 159–193.

[64] LAX, P. D., AND WENDROFF, B. Systems of Conservation Laws. *Communications on Pure and Applied Mathematics 13*, 2 (1960), 217–237.

[65] LEVEQUE, R., AND TEMPLE, B. Stability of Godunov's method for a class of 2×2 systems of conservation laws. *Transactions of the American Mathematical Society 288*, 1 (1985), 115–123.

[66] LEVEQUE, R. J. *Numerical methods for conservation laws*. Birkhauser, 1992.

[67] LEVEQUE, R. J. *Finite volume methods for hyperbolic problems*. Cambridge Univeristy Press, 2002.

[68] LIE, K.-A. Hyperbolic Conservation Laws: Computation. In *Encyclopedia of Applied and Computational Mathematics*. Springer-Verlag, 2013.

[69] LIU, X. D., OSHER, S. J., AND CHAN, T. Weighted essentially non-oscillatory schemes. *Journal of Computational Physics 115*, 1 (1994), 200–212.

[70] MACCORMACK, R. The effect of viscosity in hypervelocity impact cratering. *Journal of Spacecraft and Rockets 40*, 5 (2003), 757–763.

[71] MARTIN, J. C. Partial integration of equations of multiphase flow. *SPE Journal 8*, 4 (1968), 370–380.

[72] MISHRA, S., AND JAFFRÉ, J. On the upstream mobility scheme for two-phase flow in porous media. *Computational Geosciences 14*, 1 (2009), 105–124.

[73] NESSYAHU, H., AND TADMOR, E. Non-oscillatory central differencing for hyperbolic conservation laws. *Journal of Computational Physics 87*, 2 (1990), 408–447.

[74] NILSEN, H. M. L., HERRERA, P. A., ASHRAF, M., LIGAARDEN, I., IDING, M., HERMANRUD, C., LIE, K.-A., NORDBOTTEN, J. M., DAHLE, H. K., AND KEILEGAVLEN, E. Field-case simulation of CO_2-plume migration using vertical-equilibrium models. *Energy Procedia 4* (2011), 3801–3808.

[75] NORDBOTTEN, J. M., AND CELIA, M. A. *Geological storage of CO_2: modeling approaches for large-scale simulation*. John Wiley & Sons, 2011.

[76] NORDBOTTEN, J. M., AND DAHLE, H. K. Impact of the capillary fringe in vertically integrated models for CO_2 storage. *Water Resources Research 47*, 2 (2011), 1–11.

[77] OGUNBERU, A., AND ASGHARI, K. Water permeability reduction under flow-induced polymer adsorption. *Journal of Canadian Petroleum Technology 44*, 11 (2005).

[78] OLEINIK, O. A. Uniqueness and stability of the generalized solution of the Cauchy problem for a quasi-linear equation. *Uspekhi Matematicheskikh Nauk 14*, 2 (1959), 165–170.

[79] ROE, P. L. Some contributions to the modelling of discontinuous flows. *In Large-scale Computations in Fluid Mechanics, Proceedings of the Fifteenth Summer Seminar on Applied Mathematics,La Jolla, CA, USA, June 27 - July 8* (1985), 163–193.

[80] RUBIN, B., AND BLUNT, M. Higher-order implicit flux limiting schemes for black oil simulation. *In In proceedings of SPE Symposium on Reservoir Simulation, 17-20 February, Anaheim, California, USA* (1991).

[81] SAMMON, P. An analysis of upstream differencing. *SPE Reservoir Engineering 3*, 3 (1988), 1053–1056.

[82] Schlumberger oilfield glossary, 2014.
http://glossary.oilfield.slb.com.

[83] SHU, C.-W. Total-variation-diminishing time discretizations. *SIAM Journal on Scientific and Statistical Computing 9*, 6 (1988), 1073–1084.

[84] SUDARSHAN KUMAR, K., PRAVEEN, C., AND VEERAPPA GOWDA, G. D. Multicomponent polymer flooding in two dimensional oil reservoir simulation. 2013.

[85] TEMPLE, B. Global solution of the Cauchy problem for a class of 2x2 nonstrictly hyperbolic conservation laws. *Advances in Applied Mathematics 3*, 3 (1982), 335–375.

[86] TODD, M. R., AND LONGSTAFF, W. J. The development, testing and applicatio of a numerical simulator for predicting miscible flood performance. *Journal of Petroleum Technology 24*, 7 (1972), 874–882.

[87] TORO, E. F. *Riemann solvers and numerical methods for fluid dynamics - A practical introduction*. Springer, 1999.

[88] TRANGENSTEIN, J. A. *Numerical solution of hyperbolic partial differential equations*. Cambridge Univeristy Press, 2009.

[89] TVEIT, S., AND AAVATSMARK, I. Errors in the upstream mobility scheme for counter-current two-phase flow in heterogeneous porous media. *Computational Geosciences 16*, 3 (2012), 809–825.

[90] VALENTI, G., JESSEN, K., MALLISON, B. T., AND GERRITSEM, M. G. High-order upwind schemes for three-phase multicomponentfFlows, a preliminary investigation. *In In proceedings of SPE Annual Technical Conference and Exhibition, 26-29 September, Houston, Texas, USA* (2004).

[91] VAN GENUCHTEN, M. T. A closed-form equation for predicting the hydraulic conductivity of unsaturated soils. *Soil Science Society of America Journal 44*, 5 (1980), 892–898.

[92] VAN LEER, B. Towards the ultimate conservative difference scheme. II. Monotonicity and conservation combined in a second-order scheme. *Journal of Computational Physics 14*, 4 (1974), 361–370.

[93] VAN LEER, B. Towards the ultimate conservative difference scheme III. Upstream-centered finite-difference schemes for ideal compressible flow. *Journal of Computational Physics 23*, 3 (1977), 263–275.

[94] VAN LEER, B. Towards the ultimate conservative difference scheme. V. A second-order sequel to Godunov's method. *Journal of Computational Physics 32*, 1 (1979), 101–136.

[95] WARMING, R. F., AND BEAM, R. M. Upwind second-order difference schemes and applications in aerodynamic flows. *AIAA Journal 14*, 9 (1976), 1241–1249.

[96] YORTSOS, Y. C. A theoretical analysis of vertical flow equilibrium. *Transport in Porous Media 18*, 2 (1995), 107–129.